Monthly Notices
of the
ROYAL ASTRONOMICAL SOCIETY

MNRAS **489,** 4890–4911 (2019)
Advance Access publication 2019 September 10

doi:10.1093/mnras/stz2358

Developing a self-consistent AGB wind model – II. Non-classical, non-equilibrium polymer nucleation in a chemical mixture

Jels Boulangier [1]★ D. Gobrecht,[1] L. Decin,[1,2] A. de Koter[1,3] and J. Yates[4]

[1]*Institute of Astronomy, KU Leuven, Celestijnenlaan 200D, B-3001 Leuven, Belgium*
[2]*School of Chemistry, University of Leeds, Leeds LS2 9JT, UK*
[3]*Anton Pannenkoek Institute for Astronomy, Universiteit van Amsterdam, Science Park 904, NL-1098 XH Amsterdam, the Netherlands*
[4]*Department of Physics and AstronomUniversity College London, Gower St, London WC1E 6BT, UK*

Accepted 2019 August 22. Received 2019 August 22; in original form 2019 March 12

ABSTRACT

Unravelling the composition and characteristics of gas and dust lost by asymptotic giant branch (AGB) stars is important as these stars play a vital role in the chemical life cycle of galaxies. The general hypothesis of their mass-loss mechanism is a combination of stellar pulsations and radiative pressure on dust grains. However, current models simplify dust formation, which starts as a microscopic phase transition called nucleation. Various nucleation theories exist, yet all assume chemical equilibrium, growth restricted by monomers, and commonly use macroscopic properties for a microscopic process. Such simplifications for initial dust formation can have large repercussions on the type, amount, and formation time of dust. By abandoning equilibrium assumptions, discarding growth restrictions, and using quantum mechanical properties, we have constructed and investigated an improved nucleation theory in AGB wind conditions for four dust candidates, TiO_2, MgO, SiO, and Al_2O_3. This paper reports the viability of these candidates as first dust precursors and reveals implications of simplified nucleation theories. Monomer restricted growth underpredicts large clusters at low temperatures and overpredicts formation times. Assuming the candidates are present, Al_2O_3 is the favoured precursor due to its rapid growth at the highest considered temperatures. However, when considering an initially atomic chemical mixture, only TiO_2-clusters form. Still, we believe Al_2O_3 to be the prime candidate due to substantial physical evidence in presolar grains, observations of dust around AGB stars at high temperatures, and its ability to form at high temperatures and expect the missing link to be insufficient quantitative data of Al-reactions.

Key words: astrochemistry – methods: numerical – stars: AGB and post-AGB – stars: winds, outflows.

1 INTRODUCTION

Low- and intermediate-mass (initially 0.8–8 $M_\odot$) stars evolve through the asymptotic giant branch (AGB) phase at the end of their lifetime. During this phase, AGB stars lose vast amounts of material to their surroundings via a stellar wind and thereby contribute significantly to the chemical enrichment of the interstellar medium. As low (and intermediate) mass stars dominate the initial mass function, AGB stars are one of the main contributors of this chemical enrichment. The generally accepted hypothesis is that the mechanism triggering the onset of the AGB stellar wind is a combination of stellar pulsations and radiation pressure on newly formed dust grains (Habing & Olofsson 2004). While dynamic models incorporating this scenario can explain observed wind mass-loss rates and velocities of carbon-rich winds (Woitke 2006a), a substantial fine-tuning is needed for oxygen-rich winds (Woitke 2006b) and a model from first principles incorporating all physics and chemistry does not yet exist.

Current AGB wind models implement dust growth by accretion of gas on to tiny solid particles, so-called seeds, based on the prescription of Gail & Sedlmayr (1999). Such seed particles are either predicted using a nucleation theory (e.g. Gail & Sedlmayr 1988; Helling & Winters 2001; Woitke 2006a), or are assumed to pre-exist, typically chosen to consist of 1000 monomers or to have a radius of 1 nm (e.g. Ferrarotti & Gail 2006; Höfner et al. 2016; Dell'Agli et al. 2017). To understand the wind formation mechanism from first principles, it is essential to use a nucleation theory. However, the most

★ E-mail: boulangier.jels@gmail.com

complex nucleation theories still assume chemical equilibrium, restrict growth of nucleation clusters to addition of monomers, and apply macroscopic properties of solids to describe clusters of a few molecules. None the less, progress has been made regarding these assumptions, in a range of astrophysical fields where understanding dust formation crucial (e.g. in supernovae, brown dwarf atmospheres, and the interstellar medium). First, the assumption of chemical equilibrium is discarded by e.g. Sarangi & Cherchneff (2015), Gobrecht et al. (2016), and Sluder, Milosavljević & Montgomery (2018), who treat nucleation as consecutive chemical reactions. From a chosen cluster size, they allow dust growth by coagulation of clusters, controlled by van der Waals forces (Jacobson 2013). The chosen cluster size is typically less than five monomer units. As nucleation reaction rate coefficients are rarely known, these coefficients are often estimated and usually neglect the temperature dependence of the reaction. The latter is crucial to infer dust formation rates as a function of the radial distance from the AGB star. Secondly, the use of bulk solid properties for molecular clusters is abandoned by e.g. Köhler, Gail & Sedlmayr (1997), Goumans & Bromley (2012), Lee et al. (2015), Bromley, Gómez Martín & Plane (2016), Lee, Blecic & Helling (2018) by adopting chemical potential energies from detailed quantum mechanical calculations. When describing the clustering of gas-phase molecules it is inaccurate to use extrapolated bulk properties, such as binding energy and surface tension, first because cluster binding energies are generally significantly reduced with respect to the bulk one, and secondly because microscopic clusters do not resemble the shape/structure of the solid (Johnston 2002; Gobrecht et al. 2017; Lamiel-Garcia et al. 2017). For example, small clusters do not have well-defined surfaces like solids, rendering the use of surface tension meaningless. Thirdly, as far as we know, no astrophysical models exist where the nucleation and the growth are not restricted by specific cluster size additions (e.g. monomers or dimers). Yet polymer and more complex nucleation theories have been developed in non-astrophysics disciplines, e.g. nano and solid-state physics. Clouet (2009, and references therein) provides a good overview of different complexity levels of nucleation theory from a non-astrophysical perspective.

Presolar grains can be identified in meteorites, interplanetary particles, and cosmic dust by isotopic anomalies that cannot be explained by physical or chemical processes within the Solar system. The origin of the grains can be traced by isotopic ratios of atoms in the grains (Nittler et al. 1997) and point to other nucleosynthetic environments such as AGB stars or supernovae (McSween & Huss 2010). Here, we focus on grains with an AGB origin. Since the first discovery of a presolar Al_2O_3 grain by Hutcheon et al. (1994), several presolar oxides have been found of which the majority are Al_2O_3 grains (corundum) and only a few are $MgAl_2O_4$ (spinel) (e.g. Nittler et al. 1994; Choi et al. 1998; Nittler et al. 2008). Note that Al_2O_3 grains are often referred to as corundum, which is the thermodynamically most stable solid bulk form, yet Al_2O_3 exists in a variety of structural forms in presolar grains (Stroud, Nittler & Alexander 2004; Stroud et al. 2007). Subsequently, Nittler et al. (2008) identified the first Ti-oxides in presolar grains, however they did not have any crystallographic data that would allow to determine the structure of the grains or even conclude if they were TiO_2-grains. Later, Bose, Floss & Stadermann (2010b) claim to have found a TiO_2-grain. The occurrence of Ti-bearing presolar grains is low and their rarity is often explained by the low Ti abundance in AGB stars. Additionally, presolar silicate grains (containing Si-oxides) have been found (Nguyen & Messenger 2009; Bose et al. 2010a, 2012). A more extended summary of discovered presolar grains can be found in the Presolar Grain Database[1] (Hynes & Gyngard 2009). Besides physical evidence of presolar grains, there is also observational evidence for different dust precursors in AGB winds. Notably the 13 μm feature, which is found in spectra of half of all AGB stars (Sloan, Levan & Little-Marenin 1996; Speck et al. 2000; Sloan et al. 2003), is thought to be caused by Al_2O_3-grains (Depew, Speck & Dijkstra 2006; Zeidler, Posch & Mutschke 2013; Takigawa et al. 2015), or $MgAl_2O_4$ (Posch et al. 1999), or by SiO_2 or polymerized silicates (Speck et al. 2000). Since there is no consensus on what causes this feature, there is still a large uncertainty on the composition of dust in AGB winds.

We investigated the viability of TiO_2, MgO, SiO, and Al_2O_3 as candidates of oxygen-rich AGB dust precursors with a revised nucleation theory. We have improved on the current nucleation theories by abandoning equilibrium assumptions, discarding growth restrictions, and using quantum mechanical properties of cluster molecules. First, we evolve a nucleation system kinetically, therefore it is time dependent and not in equilibrium. Secondly, the revised theory also allows polymer nucleation (PN), not just interactions via monomers. Thirdly, quantum mechanical properties of molecular clusters are calculated with high accuracy density functional theory (DFT). Subsequently, these are used in chemical interactions between the nucleation clusters instead of using extrapolations from bulk material. The abundances and formation times of the largest nucleation clusters are examined in a closed nucleating system (no interaction with other chemical species) and in a large chemical mixture. The former assumes the monomer to be a priori present and is unable to be destroyed into smaller species. The latter allows chemical interactions between all species and starts from a purely atomic composition. To describe the chemical interactions, we used the reduced chemical reaction network of Boulangier et al. (2019) and extended this with additional reactions required to chemically couple to the nucleation candidates.

Section 2 describes the chemical evolution of a closed system and presents the improved nucleation theory. Section 3 justifies the chosen nucleation candidates and explains two different nucleation models. First, a closed nucleating model that only considers one nucleating species without interaction with other chemical species. Secondly, a comprehensive nucleating model that considers all nucleating species simultaneously in a large chemical mixture. Additionally, it elaborates on the used nucleation networks, the construction thereof, and the details of the used quantum mechanical data. Section 4 presents the results of the evolution of all nucleation candidates for the different model setups. Section 5 focuses on the implications of the model results. Section 6 discusses the limitations of the revised nucleation, the model setups, and compares the results to previous studies. Finally, Section 7 summarizes this work. The appendix consists of detailed description of used calculations (Appendices A and B) and an overview of all quantum mechanical data sources (Appendix C). Additional figures of the model results and the used chemical network are available as Appendices D and E in the Supplementary online material.

2 METHODS

This section covers the general theory of chemical reactions and how to evolve such a system, i.e. chemical kinetics (Section 2.1), and the construction of our improved non-classical, non-equilibrium PN theory (Section 2.2).

[1] https://presolar.physics.wustl.edu/presolar-grain-database

2.1 Chemistry

The evolution of the composition of a system is dictated by a set of chemical formation and destruction reactions. Mathematically, this is a set of coupled ordinary differential equations where the change in number density of the ith species is given by,

$$\frac{\mathrm{d}n_i}{\mathrm{d}t} = \sum_{j\in F_i}\left(k_j \prod_{r\in R_j} n_r\right) - \sum_{j\in D_i}\left(k_j \prod_{r\in R_j} n_r\right). \quad (1)$$

Here, the first term, within the summation, represents the rate of formation of the ith species by a single reaction j of a set of formation reactions F_i. The second term is the analogue for a set of destruction reactions D_i. Each reaction j has a set of reactants R_j, where n_r is the number density of each reactant. The rate coefficient of this reaction is represented by k_j and has units $\mathrm{m}^{3(N-1)}\ \mathrm{s}^{-1}$ where N is the number of reactants involved. To solve the chemical evolution of a system, we use the open source KROME[2] package (Grassi et al. 2014), that is developed to model chemistry and microphysics for a wide range of astrophysical applications.

In general, the rate coefficient of a two-body reaction

$$\mathrm{A} + \mathrm{B} \rightarrow \mathrm{C} + \mathrm{D} \quad (2)$$

is given by

$$k = \int_0^\infty \sigma v_\mathrm{r} f(v_\mathrm{r}) \mathrm{d}v_\mathrm{r}, \quad (3)$$

where σ is the total cross-section of an A–B collision, v_r is the relative speed between A and B, and $f(v_\mathrm{r})$ is a (relative) speed distribution. The total cross-section of a two-particle collision depends on the kinetic energy of both particles and their microphysical interactions. However, the reaction is often reduced to an inelastic collision of two hard spheres due to lack of detailed chemical information. In this case, the total cross-section is the geometrical cross-section of both spheres, $\sigma = \pi(r_\mathrm{A} + r_\mathrm{B})^2$ where r_A and r_B are the radii of both species. The speed distribution can be represented by the Maxwell–Boltzmann relative speed distribution, that considers the motion of particles in an ideal gas,

$$f(v_\mathrm{r}) = \left(\frac{\mu}{2\pi k_\mathrm{B} T}\right)^{3/2} 4\pi v_\mathrm{r}^2 \mathrm{e}^{-\frac{\mu v_\mathrm{r}^2}{2k_\mathrm{B}T}}, \quad (4)$$

where $\mu = \frac{m_\mathrm{A} m_\mathrm{B}}{m_\mathrm{A}+m_\mathrm{B}}$ is the reduced mass of the system, k_B is the Boltzmann constant, and T is the temperature of the gas. Note that when the reaction requires an activation energy E_a, the integral in equation (3) should be evaluated from the equivalent speed $v_\mathrm{a} = \sqrt{2E_\mathrm{a}/\mu}$, rather than zero. Using the geometrical cross-section and the Maxwell–Boltzmann distribution, equation (3) results in

$$k = \pi(r_\mathrm{A} + r_\mathrm{B})^2 \sqrt{\frac{8k_\mathrm{B}T}{\pi\mu}} \left(1 + \frac{E_\mathrm{a}}{k_\mathrm{B}T}\right) \mathrm{e}^{-\frac{E_\mathrm{a}}{k_\mathrm{B}T}}. \quad (5)$$

In the limit where $E_\mathrm{a} \gg k_\mathrm{B}T$ this reduces to

$$k = \pi(r_\mathrm{A} + r_\mathrm{B})^2 \sqrt{\frac{8k_\mathrm{B}}{\pi\mu}} \frac{E_\mathrm{a}}{k_\mathrm{B}} T^{-0.5} \mathrm{e}^{-\frac{E_\mathrm{a}}{k_\mathrm{B}T}}, \quad (6)$$

and has the form of a modified Arrhenius' equation,

$$k_\mathrm{Ar} = \alpha T^\beta \mathrm{e}^{-\frac{\gamma}{T}}, \quad (7)$$

where α, β, and γ are constants. In the limit where there is no activation energy or when $E_\mathrm{a} \ll k_\mathrm{B}T$, the last two terms in equation (5) reduce to 1 and the rate coefficient is given by

$$k = \pi(r_\mathrm{A} + r_\mathrm{B})^2 \sqrt{\frac{8k_\mathrm{B}T}{\pi\mu}}, \quad (8)$$

which also has the modified Arrhenius' form. Here, the last factor denotes the average relative speed, often quoted as thermal velocity.[3]

2.2 Nucleation theory

We assume that the nucleation process is homogeneous and homomolecular. The former states that there are no preferential sites for nucleation to start, and the latter means that nucleation happens by addition of the same molecular type of clusters. Heteromolecular nucleation is omitted since in this case the number of possible reactions would increase exponentially. Additionally, nucleation occurs in a pure gas-phase condition and as such no preferential nucleation sites exist. This is different compared to nucleation that can occur on solid-state surfaces that can act as a catalyst or where crystal lattice defects can reduce the energy needed for nucleation to start.

In general, a nucleation/cluster growth reaction is represented by,

$$C_N + C_M \rightarrow C_{N+M}, \quad (9)$$

where C_N and C_M are clusters[4] of size N and M, respectively. Due to a lack of reaction rate coefficients in the literature, the rate coefficient is determined via equation (8) by assuming an inelastic collision where the activation energy of the reaction is much smaller than $k_\mathrm{B}T$ and is given by

$$k^+_{N,M} = \pi(r_N + r_M)^2 \sqrt{\frac{8k_\mathrm{B}T}{\pi\mu_{N,M}}}, \quad (10)$$

where $\mu_{N,M}$ is the reduced mass of the (N, M)-system , and r_N and r_M are the radii of clusters of size N and M, respectively. Assuming that the volume scales linearly with the size of the clusters, the radii can be written as function of the monomer radius[5] r_1,

$$k^+_{N,M} = \pi(N^{1/3}r_1 + M^{1/3}r_1)^2 \sqrt{\frac{8k_\mathrm{B}T}{\pi\mu_{N,M}}}. \quad (11)$$

Note that the assumption of a spherical cluster can be generalized to a fractal cluster with a fractal radius $r_{\mathrm{f},N} = N^{1/D_\mathrm{f}} r_1$, where D_f is the fractal dimension, which equals 3 for spheres.

A cluster destruction process of an ($N + M$)-sized cluster is represented by

$$C_{N+M} \rightarrow C_N + C_M. \quad (12)$$

The rate coefficient can be derived from the principle of detailed balance which states that, at equilibrium, each elementary process is equilibrated by its reverse process. Hereby, we assume that the destruction rate is an intrinsic property of the cluster and does not depend on the embedding system (i.e. no collisional dissociation). We therefore assume that the cluster has enough time

[2] http://kromepackage.org/

[3] This is, however, not a vector quantity and naming this a velocity is therefore confusing and should be avoided. The correct terminology is average relative speed.

[4] A cluster C_N of specific size N denotes a molecule that exists of N-times molecule C, e.g. $(\mathrm{SiO})_2$ is an SiO-cluster of size 2.

[5] This assumption reduces the amount of needed information, i.e. just one molecule radius instead of N radii. It does, however, also decrease the accuracy of the description.

to relax to the lowest energy configuration between its formation and spontaneous break-up. This assumption is consistent with the fact that we describe a cluster solely by its size and minimal energy configuration. With the principle of detailed balance, the destruction rate coefficient can be determined via,

$$n^{\rm eq}_{N+M}\, k^{-}_{N,M} = n^{\rm eq}_{N}\, n^{\rm eq}_{M}\, k^{+}_{N,M},$$
$$k^{-}_{N,M} = \frac{n^{\rm eq}_{N}\, n^{\rm eq}_{M}}{n^{\rm eq}_{N+M}}\, k^{+}_{N,M}, \tag{13}$$

where $n^{\rm eq}_N$ is the equilibrium number density of the N-sized cluster and $k^{+}_{N,M}$ is the growth rate coefficient of the reversed reaction (equation 10). For a system at constant pressure and temperature, when in equilibrium, the ratio of number densities of two clusters of sizes N and M, with $N > M$, is described by

$$\frac{n^{\rm eq}_{N}\, n^{\rm eq}_{M}}{n^{\rm eq}_{N+M}} = n_{\rm tot} \exp\left(\frac{G_{N+M} - G_M - G_N}{k_{\rm B}T}\right), \tag{14}$$

where G_N is the Gibbs free energy (GFE) of an N-sized cluster and $n_{\rm tot}$ is the total number density of the gas.[6] It is more convenient to use the GFEs at standard pressure ($P^\circ = 1$ bar $= 10^5$ Pa $= 1 \times 10^6$ dyne cm^{-2}). Here, the superscript $^\circ$ refers to a quantity evaluated at this standard pressure. The GFE of a particle at any pressure can be written as a function of the standard one,

$$G = G^\circ - kT \ln\left(\frac{P^\circ}{P}\right), \tag{15}$$

because only the translational partition function is a pressure dependent term (equations A10–A9),

$$Z_t = Z^\circ_t \frac{P^\circ}{P}. \tag{16}$$

Using the standard GFE and substituting equation (15) into equation (14) results in,

$$\frac{n^{\rm eq}_{N}\, n^{\rm eq}_{M}}{n^{\rm eq}_{N+M}} = \frac{P^\circ}{k_{\rm B}T} \exp\left(\frac{G^\circ_{N+M} - G^\circ_M - G^\circ_N}{k_{\rm B}T}\right). \tag{17}$$

Substituting this ratio into equation (13) yields a cluster destruction rate coefficient

$$k^{-}_{N,M} = k^{+}_{N,M} \frac{P^\circ}{k_{\rm B}T} \exp\left(\frac{G^\circ_{N+M} - G^\circ_M - G^\circ_N}{k_{\rm B}T}\right). \tag{18}$$

Note that the standard GFEs are often given in kJ mol^{-1}, in which case the Boltzmann constant $k_{\rm B}$ in the exponential has to be replaced with the universal gas constant R in kJ K^{-1} mol^{-1}.

3 MODEL SETUP

This section explains the two different nucleation descriptions that have been used, a monomer and polymer one (Section 3.1). Next, it justifies the choice of nucleation candidates that have been considered, namely TiO_2, MgO, SiO, and Al_2O_3 (Section 3.2). Additionally, it describes the two different types of chemical nucleation networks, a closed one and a comprehensive one (Sections 3.3 and 3.4). The closed nucleating network assumes the monomer to be a priori present and is unable to be destroyed into smaller species. No assumptions have been made on how the monomer has been formed or its possible existence. The comprehensive nucleating network does not assume the existence of the nucleating monomers and starts from a purely atomic composition. The (possible) formation of the nucleating monomers and other chemical species is determined by a large chemical reaction network. Finally, this section summarizes all the additionally gathered data and performed calculations prior to running the nucleation models (Section 3.6).

3.1 Nucleation description

We consider two different nucleation descriptions, polymer and monomer nucleation (MN). The former is the most general and uses growth and destruction of the corresponding clusters described by equations (11) and (18), whereas the latter uses those same equation but with $M = 1$ reducing it to a monomer. We make this distinction because, to our knowledge, most homomolecular nucleation studies assume MN (e.g. Köhler et al. 1997; Lee et al. 2015; Bromley et al. 2016; Lee et al. 2018). However, the monomer assumption is only valid when the number of monomers is much larger than that of any other cluster. There is no quantitative evidence to support this assumption and it turns out to be invalid in our parameter space[7] (Section 4). Sarangi & Cherchneff (2015), Gobrecht et al. (2016), and Sluder et al. (2018), however, do allow PN but limit it to small clusters ($N < 5$).

3.2 Nucleation candidates

In oxygen-rich atmospheres (C/O < 1), carbon is predominantly locked-up in CO, strongly inhibiting the formation of carbonaceous dust. Highly stable molecules in a carbon-deficient gas such CO, N_2, and CN only have a solid form (ice) at temperatures well below 500 K. Also solid oxygen only forms at extremely cold temperatures. Hence, nucleation at high temperatures must proceed via hetero-atomic species such as composite metal[8] oxides. Monomers with high bond energies[9] are preferential candidates for first nucleation because higher energies generally allow for easier formation and more difficult destruction at higher temperatures. Therefore, bond energies of simple metal oxides give a hint for which molecules will play a predominant role. Considering the most abundant atomic metals in AGB winds, SiO, TiO, and AlO are the metal oxides with the highest bond energy (Fig. 1). Even though the amount of Ti is almost a factor 40 and 400 lower than Al and Si, respectively, it can still be an important molecule due to its high bond energy. Similarly, MgO, and FeO have lower bond energies but the high atomic abundance of Mg and Fe can make them important nucleation candidates.

Although the metal oxides hint at the engaged species, the most compelling evidence for nucleation building blocks comes from presolar grains. Considering all the presolar grains that originated from AGB stars, Al_2O_3 grains are the most frequently occurring oxygen-bearing ones (Hutcheon et al. 1994; Nittler et al. 1994; Choi et al. 1998; Nittler et al. 2008). In these grains, Al_2O_3 is the basic building block (repeating formula unit) that forms the bulk grains with a variety of structural forms (Stroud et al. 2004, 2007). The repetition of such a basic building block strengthens our assumption of homomolecular nucleation. The second most frequently found grains, roughly a factor 7 less abundant, are the

[6] Note that this is only valid in the dilute limit, i.e. the number of clusters is small compared to the total number of particles.

[7] For higher densities this will be even less valid, e.g. brown dwarfs and planetary atmospheres.

[8] We refer to the chemical use of *metals* and not the astronomical one.

[9] Bond energy is a measure of the strength of a chemical bond.

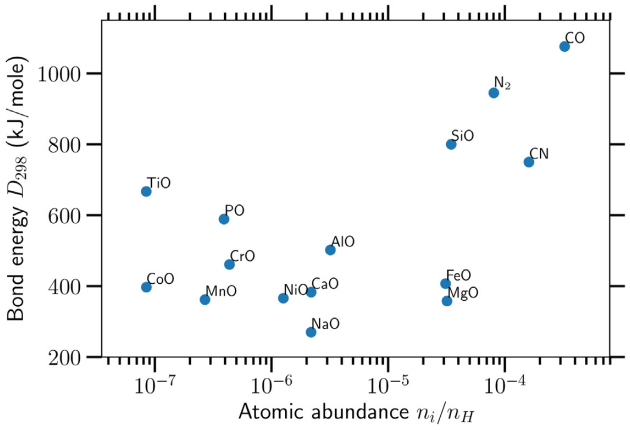

Figure 1. Simple molecules (mainly oxides) with high bond energies at 298 K (Luo 2007) and/or a high atomic abundance provide hints at which species play a dominant role in the initial dust formation in AGB winds.

Table 1. Initial chemical composition. This is equal to the time-averaged mass fractions in the wind for a nucleosynthetic AGB evolutionary model with an initial mass of 1 $M_\odot$ and metallicity $Z = 0.02$ of Karakas (2010). The mass fraction of Ti is that of solar abundance (Asplund et al. 2009).

Element i	Mass fraction X_i	$n_i/n_{\rm H}$
He	3.11×10^{-1}	1.16×10^{-1}
C	2.63×10^{-3}	3.26×10^{-4}
N	1.52×10^{-3}	1.61×10^{-4}
O	9.60×10^{-3}	8.92×10^{-4}
F	4.06×10^{-7}	3.18×10^{-8}
Na	3.38×10^{-5}	2.18×10^{-6}
Mg	5.16×10^{-4}	3.19×10^{-5}
Al	5.81×10^{-5}	3.20×10^{-6}
Si	6.54×10^{-4}	3.47×10^{-5}
P	8.17×10^{-6}	3.92×10^{-7}
S	3.97×10^{-4}	1.84×10^{-5}
Ti	2.84×10^{-6}	8.44×10^{-8}
Fe	1.17×10^{-3}	3.16×10^{-5}
e^-	0	0
H	$1 - \sum_i^N X_i$ $= 6.72 \times 10^{-1}$	1

ones with $MgAl_2O_4$ as repeating formula unit (Nittler et al. 1994; Choi et al. 1998; Nittler et al. 2008). Additionally, there is some evidence for silicon and titanium oxides in presolar grains (Nittler et al. 2008; Nguyen & Messenger 2009; Bose et al. 2010a,b). However, as only little amount of this material is detected, it is unclear what the repeating basic building block is.

Considering the occurrence in presolar grains, the atomic metal abundance, and the bond energy of simple metal oxides, we choose Al_2O_3 to be our primary nucleation candidate. Next, we do not consider $MgAl_2O_4$ as a candidate as this molecule consist of three different atoms, making it more complex to characterize its molecular features. We include MgO as a candidate because it (and its clusters) might play a role in the formation of $MgAl_2O_4$ grains. Additionally, we take TiO_2 as a nucleation candidate. Even though there is no substantial evidence for TiO_2 to be the repeating formula unit in presolar grains containing titanium oxides, it is, however, the repeating basic building block in other commonly found titanium minerals on Earth (e.g. rutile and anatase). Lastly, we select SiO as a candidate. Although there is no physical evidence in presolar grains that SiO is the repeating formula unit, it does have the highest bond energy of the most abundant atomic metals and it most likely will play an important role in the formation of silicate grains. We exclude FeO from this study because, so far, only one potential detection of FeO in AGB circumstellar environment has been reported (Decin et al. 2018), nor has there been proof of FeO-containing particles in presolar grains. Additionally, Fe-containing nanoparticles can display various magnetic behaviours such as ferromagnetic, antiferromagnetic, ferrimagnetic, and non-magnetic, and are therefore challenging to characterize.

A typical interstellar dust grains of radius 0.1 μm contains 10^9 monomer units with a typical radius of roughly 0.1 nm (Table C1). Hence, in order to construct a dust grain via reaction rate equations, one needs of the order of 10^9 equations. As this is computationally impossible, we limit the maximum cluster size so the largest clusters roughly consist of 20–40 atoms, making it still feasible to perform high accuracy DFT calculations (Section 3.6.2). We take the largest cluster to be $(TiO_2)_{10}$, $(SiO)_{10}$, $(MgO)_{10}$, and $(Al_2O_3)_8$. Note that these cluster sizes are not necessarily the threshold from which the species can be considered as a macroscopic, solid dust grain (Section 6).

3.3 Closed nucleation networks

A closed nucleation model corresponds to the evolution of a cluster system according to growth and destruction rate coefficients (equations 11 and 18) with the monomer as the smallest and the maximally considered cluster size as the largest allowed clusters. Such a model starts with an initial monomer abundance and follows the growth of this monomer over time at a fixed temperature. We construct a model grid in temperature and density that is primarily applicable to an AGB wind (but that is also valid in other environments) and evolve each model over a time-scale of 1 yr. The latter corresponds to the longest dynamically stable period (between pulsation-induced consecutive shocks), resulting in a roughly constant local temperature and density in that period. For the initial abundance of the monomer we assume all of the available atomic metal[8] to be locked-up in the monomer (Table 1). For the available atomic metal abundance we choose the same composition as Boulangier et al. (2019), who take the time-averaged elemental mass fractions in the wind from 1 $M_\odot$ and $Z = 0.02$ AGB evolution model of Karakas (2010) [defined as $\langle X(i) \rangle$ in Karakas & Lattanzio (2007)]. For Ti we take the solar abundance because this element is not considered in the nucleosynthesis networks of Karakas (2010).[10]

3.4 Comprehensive chemical nucleation network

A comprehensive nucleation model corresponds to the evolution of nucleation clusters in a large chemical network according to growth and destruction rate coefficients (equations 11 and 18) until a specified maximum cluster size. Such a model starts from the atomic composition rather than the initial monomer abundance that is used in a closed nucleation model (Section 3.3). This is a more realistic prescription as is removes the assumption of the monomer being (abundantly) present. Moreover, it allows for more chemical interaction between species and the creation of other metal-bearing

[10]The abundance of Ti is not affected by the slow neutron capture process because of low neutron capture cross-sections for elements below iron, and burning temperatures are not high enough for higher burning processes to affect Ti. Hence, $\langle X(i) \rangle$ of Ti does not change between birth and death of low- and intermediate-mass stars.

molecules besides the nucleation candidate clusters. In practice, the reaction network consists of the closed nucleation networks of TiO_2, MgO, SiO, and Al_2O_3 (Section 3.3) extended with the reduced AGB wind network of Boulangier et al. (2019). However, because their reduced network does not consider any Ti, Al, and only a few Mg reactions, we have added all reactions that include these elements available in the literature. Additionally, where necessary and possible, we have included the reversed reaction based on the assumption of detailed balance.[11] As with the closed nucleation models, we compute the same grid of models in temperature and density over a 1 yr period but with an initial atomic composition (Table 1).

3.5 Justification of nucleation networks

It is instructive to investigate the nucleation of chemical species in a closed system with the assumption of an a priori monomer existence to gain insight in the efficiency of the nucleation process different species. Such preliminary nucleation investigations can already exclude candidates as viable AGB dust precursors based on inefficient nucleation at high temperatures. This pre-selection of nucleation candidates leads to a considerable reduction of the computational cost when coupling the reaction network to a hydrodynamical framework. Moreover, a closed nucleation investigation reduces the number of uncertainties when interpreting the nucleation process. For example, the nucleation of clusters in a large chemical network might not occur due to an insufficient or incorrect description of the gas-phase chemistry prior to the monomer formation rather than the nucleation process itself, which can be very effective. By ignoring the disentanglement between monomer formation and the nucleation process, the nucleation species can be wrongly discarded as a good dust candidate. Additionally, the closed nucleation system allows us to investigate the impact of using the improved nucleation description, such as MN versus PN and using molecular energies compared to bulk energies.

3.6 Construction of nucleation networks

This section covers the additional chemical reactions, quantum mechanical properties and calculations needed to construct valuable nucleation reaction networks. The first section describes the addition of chemical reactions and the second section the collection and calculation of quantum mechanical properties of molecules and clusters necessary for certain reversed reactions.

3.6.1 Additional reactions

In order to construct a reaction network for the comprehensive nucleation models, reactions from atomic Ti, Al, Si, and Mg up to the corresponding nucleation monomer have to be included. Additionally, to increase the accuracy of chemical interactions, as many as possible other nucleation-related metal-bearing molecules should be added to the network with corresponding reactions. Even though some species or reactions might not be important and could be omitted, such filtering is beyond the scope of this paper because computation time is currently not an issue as we only perform grids of models rather than coupling it in real-time to a hydrodynamical framework.

Ti-bearing molecules are not well studied and corresponding reaction rate coefficients are lacking in astrochemical data bases. We could only find nine reactions of which only one had a reversed reaction. For the remaining eight reversed reactions we assumed detailed balance. We did, however, ignore reactions for the Ti–Cl–H system (Teyssandier & Allendorf 1998) due to the low abundance of both Cl and Ti in AGB stars.

Apart from the SiO-nucleation reactions, just one other Si-reaction is added relative to Boulangier et al. (2019), whose network is mainly constructed from the astrochemical data bases UMIST (McElroy et al. 2013) and KIDA (Wakelam et al. 2012) in which Si-bearing molecules are well studied. The destruction of SiO_2 by atomic hydrogen, calculated via detailed balance, is added to the chemical network to equilibrate the forward reaction. Previously, the only incorporated SiO_2 destruction reaction was the collision of He^+, which requires very high temperatures.

Additionally, 15 Mg-related reactions are added. Only for seven of them we added a reversed detailed balance reaction. However, due to a lack of quantum chemical data on MgO_2, MgO_3, and MgO_4 no reversed reactions for reactions including such species are added. Reactions with ionized Mg-bearing molecules can be found in the literature (Martínez-Núñez et al. 2010; Whalley & Plane 2010; Whalley et al. 2011) but are ignored because ionization is unlikely at the low temperatures of our grid.

In total 51 Al-related reactions and their reversed detailed balance reactions are added that mostly originate from combustion chemistry.

3.6.2 Quantum mechanical properties

In order to calculate the reversed reaction rate coefficient under the assumption of detailed balance, one needs the GFE of all reactants and products, as a function of temperature at a specific pressure[12] [equation 18 for nucleation and e.g. equations 73−76 in Grassi et al. (2014) in general]. In principle, one can also use the difference in Gibbs free energy of formation (GFEoF) because the additional contribution of individual atoms cancels out (Appendix B). On one hand, using the GFEoF has the advantage of being calculated for numerous species and being included in different data bases, e.g. so-called NASA-polynomials[13] (Burcat & Ruscic 2005) and NIST-JANAF Thermochemical Tables[14] (Chase 1998). On the other hand, there are inconsistencies between both data bases such as the same species having different GFEoF values. By benchmarking, Tsai et al. (2017) also came to this conclusion and assign the discrepancies between the data bases to a differently defined reference level that corresponds to zero energy. Another reason might be that the GFEoF values rely on experimentally determined values of quantities at room temperature that can have large error bars. Moreover, the details of the calculations or experiments are often unclear as these have been performed decades ago and frequently lack detailed descriptions. For consistency, we use (and strongly encourage to use) GFE rather than GFEoF. Because the GFE is an intrinsic property of a species, it does not rely on any experimental value at a reference temperature (e.g. room temperature) but can be calculated from first principles with absolute zero as a reference

[11] The reversed rate coefficient depends on the difference in GFE of reactants and products (i.e. the GFE of reaction). If there was insufficient data in the literature to calculate these energy values, we did not include the reversed reaction.

[12] One only needs to determine the GFE at a single pressure to be used in reversed rate coefficients. Often a standard pressure of 1 bar $= 1 \times 10^5$ Pa is used.

[13] http://garfield.chem.elte.hu/Burcat/burcat.html

[14] https://janaf.nist.gov/

point (Appendix A). In short, to calculate the GFE as a function of temperature, one only needs the total partition function and the electronic potential energy at zero Kelvin (equation A9).

We calculate the GFE of all clusters of the four nucleation species TiO_2, MgO, SiO, and Al_2O_3 by first gathering the most recent structural information (i.e. atomic coordinates) of the lowest energy isomers, i.e. the so-called global minima (Table C1). Subsequently, using GAUSSIAN09 (Frisch et al. 2013), we perform DFT calculations including a vibrational analysis to determine the GFE. For consistency, we always use the same functional and basis set, namely the B3LYP functional (Becke 1993) and 6-311+G*[15] basis set. Other functionals and/or basis sets might be more accurate for specific properties or species, yet B3LYP is well established and suitable for inorganic oxides (Corà 2005), and 6-311+G* is a good compromise between accuracy and computation time.

For all non-cluster species participating in reversed reactions, we have collected the electronic potential energies when available (Table C2). All energies originate from DFT calculations by the Computational Chemistry Comparison and Benchmark DataBase[16] (CCCBDB; Johnson 2018). For consistency we always use results of the same functional and basis set, namely B3LYP and 6-31+G**.[17] We perform DFT calculations for the species of which no electronic potential energies are present in any data base, using the same DFT setup as for the nucleation clusters (Table C2).

When possible, we have gathered partition functions[18] of the non-cluster species participating in reversed reactions (Table C2). These values originate from detailed calculations and/or experiments. If no literature partition functions could be found, we have calculated them from internal energy levels (rotational, vibration, and electronic[19]) found in the CCCBDB (Appendix A). Note that this method is less precise due to approximations such as considering the species as a rigid rotor and harmonic oscillator. Again, when no energy levels were available in the literature, we have calculated them via a vibrational analysis as a follow-up on the DFT calculations (Table C2).

4 RESULTS

This section presents the simulation results of the two main model setups, one with closed nucleation networks and one with a comprehensive chemical nucleation network. The closed nucleation network setup considers four nucleation species, TiO_2, MgO, SiO, and Al_2O_3. Additionally, each of these sub-setups will use the MN and the PN approach. The comprehensive chemical nucleation network setup will encompass all four mentioned nucleation species but only use the PN approach.

Because our results include four parameters (temperature, gas density, cluster number density, and time), we reduce the dimensionality to analyse the outcome. The analysis of the cluster size distributions in (T, ρ)-space is limited to the end of the simulation, i.e. after 1 yr. Subsequently, to infer temporal effects, we choose a benchmark constant total mass density of 1×10^{-9} kg m^{-3}, which is a typical value we expect in an AGB wind (fig. 10, Boulangier et al. 2019). Note that we use the total mass density of the gas as a parameter since this value remains constant as compared to the total number density.

4.1 Closed nucleation networks

This section covers the evolution of four nucleation species TiO_2, MgO, SiO, and Al_2O_3 for a closed nucleation network setup with both the MN and the PN description. To ensure the overview, we mainly discuss the largest clusters because they are most interesting to understand formation of macroscopic dust grains. Additional figures for all clusters can be found in Appendix D1.

4.1.1 TiO_2

$(TiO_2)_{10}$ forms when the temperature drops below the sharp threshold at 1000 to 1200 K, where the low (high) temperature threshold is for the lowest (highest) densities (Fig. 2). At temperatures above 1200 K, its abundance drops orders of magnitude (Figs D1 and D10). As expected, a higher density leads to more collisions facilitating nucleation at higher temperatures. Between roughly 950 K and the upper temperature threshold for both MN and PN, almost all of the available monomers end up in $(TiO_2)_{10}$ (>80 per cent). However, using MN or PN yields vastly different results at low temperatures. In this regime, roughly below 950 K, the abundance of $(TiO_2)_{10}$ drops orders of magnitude in the case of MN in contrast to PN, where its abundance is nearly identical and accounts for 40–50 per cent of the available titanium. The low abundance in the MN case is caused by a relatively rapidly developing lack of monomers in this temperature range, because, by design, growth is only allowed by the addition of monomers. Once the bulk of the material is clustered in $N = 2$–4 chains, the monomer population becomes depleted and further growth is quenched (Fig. D1). At our benchmark density of 1×10^{-9} kg m^{-3}, this typically happens in less than a day. This bottleneck does not occur in the case of PN since, by design, all clusters are allowed to participate in the growth process (Fig. D10). Therefore, even in the case of a lack of monomers other small clusters can interact and form larger clusters. In this low-temperature regime, this occurs so efficiently that the small clusters ($N = 2$–4) are completely depleted and turned into large clusters. The fact that clusters of intermediate ($N > 6$) size are still present is somewhat artificial since they are only allowed to grow by addition of smaller ones due to the limitation of a maximum size of $N = 10$. As these small clusters are already depleted, the intermediate growth is quenched. In reality clusters of size $N = 6$ and $N = 7$ can interact to form an $N = 13$ sized cluster.

Using MN, the abundance of the largest molecules converges[20] slowest, roughly after 20 and 60 d for $(TiO_2)_9$ and $(TiO_2)_{10}$, respectively. All smaller molecules roughly converge after 20 d or less (Fig. D2). Using PN, the convergence of $(TiO_2)_{10}$ occurs faster, already after 20 d, even in less than 1 d for the slightly smaller clusters. All small clusters are also formed within 1 d but continue to steadily grow into larger ones (Fig. D11).

[15] This basis set is spanned by six primitive Gaussians, includes diffusion(+) and polarization(*).

[16] https://cccbdb.nist.gov/

[17] CCCBDB does not contain calculations with 6-311+G*, the one we used for the nucleation clusters. The 6-31+G** basis set is slightly smaller but also includes diffusion and polarization, and most closely resembles 6-311+G*.

[18] Note that this excludes the translational part because that depends on the number of particles and the pressure for which one wants to calculate the total partition function.

[19] The number of electronic energy levels is truncated to be valid below ~ 10 000 K, which is more than sufficient for the purpose of this paper.

[20] This happens over the entire temperature range unless stated otherwise.

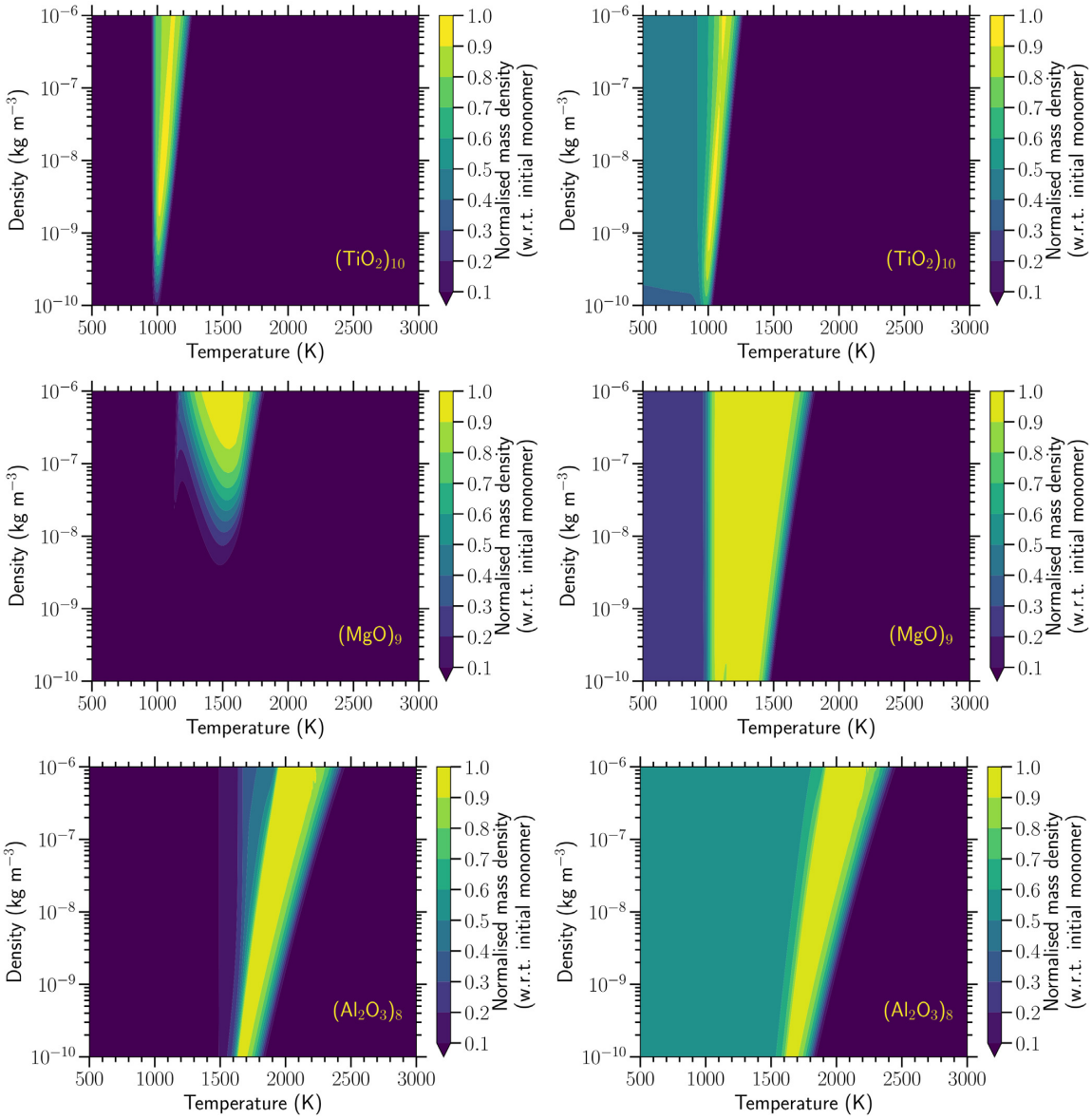

Figure 2. Normalized mass density (or mass fraction) w.r.t. the initially available monomers after 1 yr of $(TiO_2)_{10}$, $(MgO)_9$, and $(Al_2O_3)_8$ for the closed nucleation models with left MN and right PN description. We refrain from showing $(SiO)_{10}$ since its abundance is zero in the entire parameter space. Note that $(MgO)_9$ is the second largest cluster, but most stable and more abundant one. MN under predicts the amount of large clusters at low temperature, as compared to PN. This under prediction is due to the limitation of growth-by-monomers in the MN description. In the most favourable nucleation conditions, more than 90 per cent of the initial monomers end up in the largest cluster. Al_2O_3-clusters are the primary candidate for first dust precursors because $(Al_2O_3)_8$ forms at the highest temperature as compared to the other candidates. Normalized number densities w.r.t. the initially available monomers can easily be found by dividing the normalized mass density by the cluster size, i.e. divide by 8 in the case of $(Al_2O_3)_8$. An overview of all clusters of all candidates can be found in Appendix D1 with an in-depth analysis in Sections 4.1 and 5.2.

4.1.2 MgO

Unlike for TiO_2 clusters, the conditions that determine the presence of the largest MgO-cluster differ strongly between the different nucleation descriptions, being more complex in the MN case. Yet both nucleation descriptions reveal that the second largest cluster $(MgO)_9$, rather than the largest cluster $(MgO)_{10}$, is the most stable and therefore most abundant cluster (Figs D3 and D12). Hence, we mainly discuss $(MgO)_9$. In the MN case, between 1100 and 1500 K and at the highest densities all available monomers end up in $(MgO)_9$ (Fig. 2). But, within this temperature range, this amount strongly decreases with decreasing density where at 1×10^{-8} kg m^{-3} just 10 per cent ends up in $(MgO)_9$ and at the lowest densities this amount reduces to 0.01 per cent (Fig. D3). Note that below 1100 K $(MgO)_9$ clusters can also exist but maximally take up 1 per cent of the available monomers. In the PN case, $(MgO)_9$-clusters already form below 1500–1700 K and above 1000 K they contain over 90 per cent of the available monomers (Fig. 2). Below 1000 K, they are less abundant but still encompass between 20 and 30 per cent of the monomers. Note that below 1000 K, there is more $(MgO)_{10}$ than $(MgO)_9$, making the largest cluster the most stable one at low temperatures (Fig. D12). Similar to the other nucleation candidates, the lack of large MgO-clusters at low temperatures,

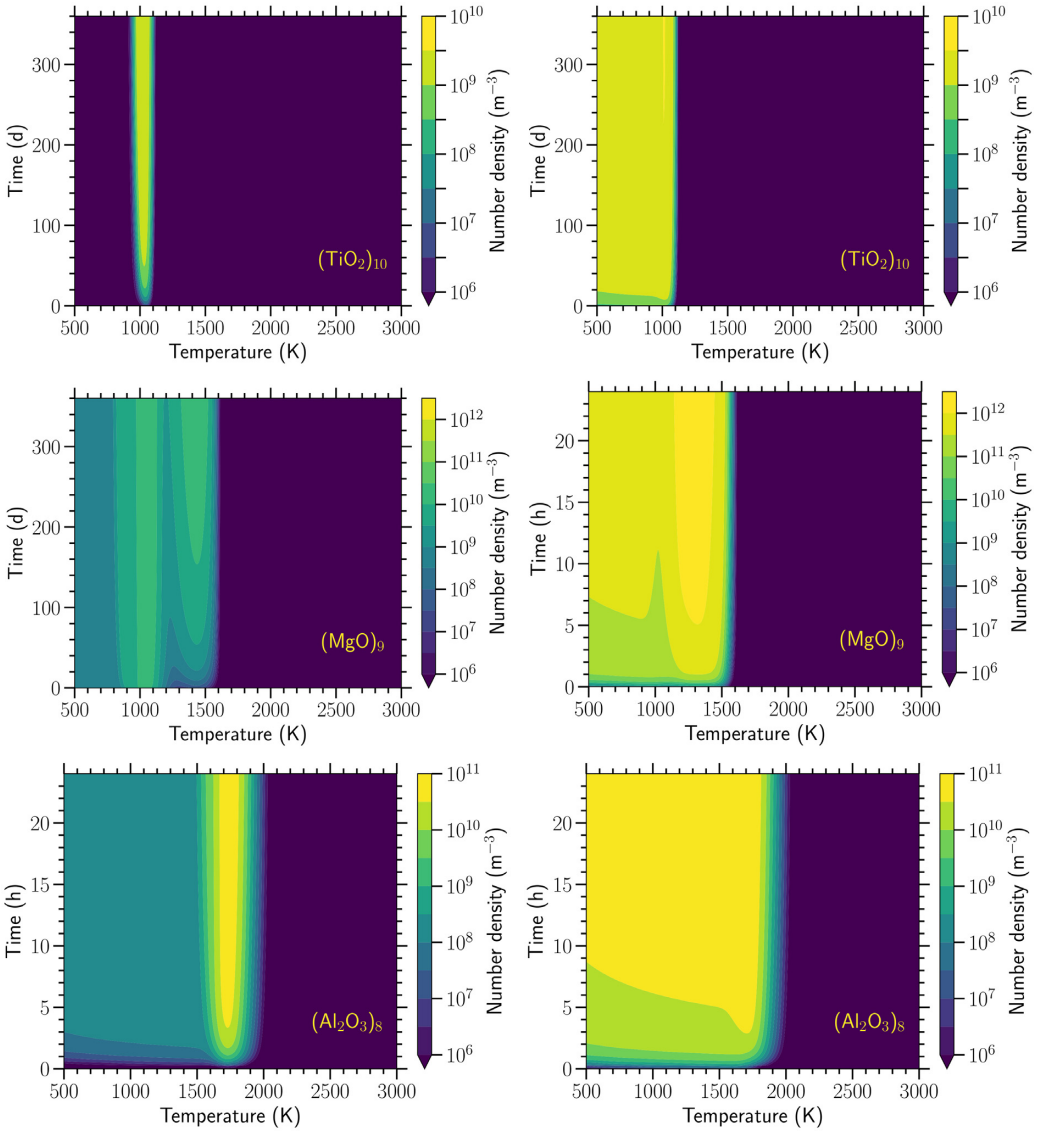

Figure 3. Temporal evolution of the absolute number density of $(TiO_2)_{10}$, $(MgO)_9$, and $(Al_2O_3)_8$ at the benchmark total gas density $\rho = 1 \times 10^{-9}\,\mathrm{kg\,m^{-3}}$ with left MN and right PN description. Be aware of the different time-scales between species. Overall, convergence with MN description takes slightly longer than using the PN one. It can also yield vastly different final abundances that are most noticeable for $(MgO)_9$. We refrain from showing $(SiO)_{10}$ since its abundance is zero in the entire parameter space. An overview of all clusters of all candidates can be found in Appendix D1 with an in-depth analysis in Sections 4.1 and 5.2.

below 1000 K, in the MN case is due to the construction of this nucleation description that limits growth by addition of monomers. It is also interesting to note that in both nucleation cases and above 1000 K, cluster sizes $N = 2, 4, 6$, and 9 are more abundant than their direct size-neighbours. This is a consequence of the energetic stability of these MgO-cluster sizes. This phenomenon would not arise when using extrapolated bulk properties for the clusters (i.e. classical nucleation), but only when calculating the energy on a microscopic level (i.e. quantum mechanically).

Determining the time-scale of abundance convergence for MgO-clusters is problematic, due to the complex behaviour in temperature–space. We give a rough convergence time-scale below and above 1000 K. Below 1000 K and in the case of MN, all clusters converge in just a few hours (Fig. D5). In the case of PN, the largest clusters do converge in a few hours but smaller clusters form in less than a few hours and then gradually get destroyed again over the course of a few days before reaching convergence (Fig. D14). $(MgO)_5$ stands out as its abundance still gradually changes on time-scales of 10–100 d (Fig. D13). Because the evolution above 1000 K is less straightforward, we limit the analysis to the largest most stable cluster $(MgO)_9$, and refer the reader to Figs D4, D5 and D13, D15 for more details on all clusters. In the case of MN, the abundance of $(MgO)_9$ converges after roughly 180 d, whereas using PN this happens in only a few hours (Fig. 3).

4.1.3 SiO

In both nucleation cases, the largest SiO-clusters do not form significantly in our (T, ρ)-range (Figs D6 and D15). Between 500 and 700 K most monomers end up in $(SiO)_3$ and remain in the monomer above this temperature. Note that sizes $N = 5$–9 do not form at all. Since no large clusters form in our (T, ρ)-range, we refrain from analysing any time dependence.

4.1.4 Al_2O_3

For both nucleation descriptions, the largest Al_2O_3-clusters already form at temperatures as high as 1800–2400 K, depending on the total gas density (Fig. 2), i.e. in hotter regimes than any of the other nucleation candidates. Moreover, between 1600–1700 and 1900–2200 K more than 90 per cent of the available monomers are locked-up in the largest cluster $(Al_2O_3)_8$. Between the lower limits and 1500 K, $(Al_2O_3)_8$ encompasses between 10 and 90 per cent of the available material for the MN description. Below 1500 K, MN again impedes a subsequent growth because the monomers are depleted once small clusters have formed, resulting in a pile-up of small clusters unable to continue to grow (Fig. D7). PN does not have this limitation and $(Al_2O_3)_8$ contains more than 50 per cent of the available monomers in the entire temperature range below the formation threshold. Additionally PN growth is so efficient that the bulk of the material grows to sizes above $N = 5$, removing all smaller clusters (Fig. D16).

In both nucleation cases, the formation of $(Al_2O_3)_8$ happens so fast that it is invisible on a time-scale of days (Figs D8 and D17). Refining the time sampling reveals that, in both nucleation cases, convergence of the abundance of $(Al_2O_3)_8$ already occurs after roughly 5–10 h (Fig. 3). For MN, convergence happens even faster for smaller clusters (Fig. D9). For PN, however, there is a gradual creation and destruction of the smaller clusters, on a time-scale of hours (Fig. D18). Even on a time-scale of 100 d, the smallest clusters do not converge but gradually get converted to larger ones (Fig. D17).

4.1.5 Comparison with equilibrium compositions

The equilibrium abundance ratio of two clusters with different sizes w.r.t to the equilibrium abundance ratio of two other cluster sizes can be calculated via equation (17). Such ratio of ratios can be used to more quantitatively discuss if clusters distributions have reached the equilibrium composition. Since it is most meaningful to compare ratios if nucleation is feasible, the ratios of two smaller clusters w.r.t. the ratio of the two largest clusters are discussed in the favourable temperature range. The results, shown for comparison with the equilibrium abundances, correspond to the closed PN models for the benchmark total gas density $\rho = 1 \times 10^{-9}\,\mathrm{kg\,m^{-3}}$ at the final time-step (1 yr). Note that if the number density of any of the four clusters species is below the numerical solver accuracy of $1 \times 10^{-20}\,\mathrm{cm^{-3}}$, the ratios are not shown.

The relative abundances ratios of TiO_2- and MgO-clusters do not reach the equilibrium ratios in the entire temperature range (Figs D19 and D20). At the highest temperatures, at which the nucleation is feasible, the model results correspond to the equilibrium ratios. However, at lower temperatures, the clusters need more time to reach the equilibrium ratios since the interaction probability is lower. This transition is visible between 900–1000 and 1000–1300 K for the TiO_2- and MgO-clusters, respectively. The fact that the clusters have not yet reached equilibrium ratios is also visible from the temporally changing abundances in Figs D11 and D13. The relative abundance ratios of Al_2O_3-clusters deviate more from the equilibrium ratios (Fig. D21). Due to the large variation in number densities of the clusters in different temperature regimes (order of magnitude), it is often impossible to compare ratios of the Al_2O_3-clusters. This variation is more clearly visible in Fig. D17. SiO-clusters are not discussed since they do not significantly form in the temperature range of interest.

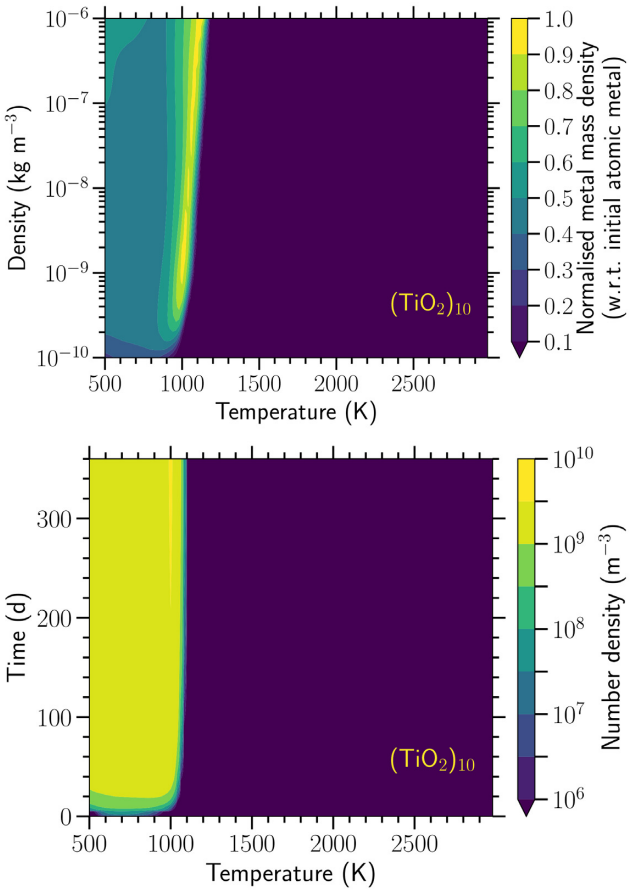

Figure 4. Normalized mass density after 1 yr (top) and temporal evolution of the absolute number density at the benchmark total gas density $\rho = 1 \times 10^{-9}\,\mathrm{kg\,m^{-3}}$ (bottom) of $(TiO_2)_{10}$ for the comprehensive chemical nucleation models using the PN description. The results are similar to the closed nucleation model (Fig. 2) where $(TiO_2)_{10}$ forms from 1000 to 1200 K and converges within roughly 20 d. The largest cluster encompasses more than 90 per cent of the available Ti, in the most favourable nucleation conditions. This implies that all atomic Ti quickly forms TiO_2 that subsequently starts to nucleate, in favourable conditions. An overview of all Ti-bearing molecules can be found in Appendix D2 with an in-depth analysis in Sections 4.2 and 5.2.

4.2 Comprehensive chemical nucleation network

This section covers the evolution of the four nucleation species TiO_2, MgO, SiO, and Al_2O_3 for a comprehensive chemical nucleation network with the PN description. To ensure the overview, we mainly discuss the species that also contain the cluster metals (Ti, Mg, Si, and Al) because they are most interesting to understand formation of macroscopic dust grains. In analogy with Section 4.1, only the temporal evolution of the nucleation clusters is presented. Additional figures for all species of interest can be found in Appendix D2.

4.2.1 TiO_2

The formation of $(TiO_2)_{10}$ occurs at the same temperature and density conditions as in the closed nucleation model with the PN approach, i.e. when the temperature drops below the sharp threshold at 1000–1200 K (Fig. 4). Above this threshold, Ti resides in either TiO_2, TiO, or remains atomic, with the atomic state preferred at the

highest temperatures (above 2000 K or higher for higher densities) (Fig. D22). The convergence of $(TiO_2)_{10}$ happens within roughly 40 d, similar to the closed nucleation model with PN (Fig. 4). The convergence of other TiO_2-clusters is also similar to the closed PN case (Fig. D23).

4.2.2 *MgO*

All available Mg remains atomic. Neither MgO, nor the MgO-clusters, nor any Mg-bearing molecules are formed. Hence, we refrain from showing the abundance figures.

4.2.3 *SiO*

The abundance evolution of all SiO-clusters, in temperature, density, and time, is the same as for the closed nucleation PN model, i.e. the large clusters do not form in the considered temperature–density range and the smallest clusters only form at the lowest temperatures (Fig. D24). Above roughly 700 K, all Si is locked-up in the SiO_2 molecule (except at the highest temperatures and lowest densities, which is due to time constraints of the simulation). This finding is somewhat in contrast to the higher binding energies of SiO compared to SiO_2 (Section 6.1.2). Below 700 K, the most abundant molecules are SiO and $(SiO)_3$. Note that in the entire (T, ρ)-grid, Si does not remain atomic.

4.2.4 *Al_2O_3*

Most of the Al remains atomic except for some specific (T, ρ)-combinations. Overall creation of Al-molecules is up to maximally 1 per cent of the total available Al, except at the lowest temperatures for both extremes in the considered density range where it can be up to roughly 50 per cent (Fig. 5). The most abundant molecules are AlO, AlH, $Al(OH)_2$, and $Al(OH)_3$. Their formation regimes can be recovered in the abundance figure of Al, and only AlO forms in the entire temperature range. Note that the figures of less abundant Al-bearing molecules are only shown in Appendix D2 since their abundance never exceeds the chosen threshold (Fig. D25).

5 IMPLICATIONS OF RESULTS

This section interprets the nucleation model results and what they implicate for AGB dust precursors. Be aware that conclusions drawn from closed nucleation networks are based on the underlying assumption that the monomer exists and that all of the nucleation-related metal is turned into the monomer. The reader should be cautious when using these results as they are not necessarily physical. They are, however, useful in their own right to investigate the efficiency of individual nucleation species and the improved nucleation description.

5.1 Closed nucleation networks

The most prominent result is that large Al_2O_3-clusters can form fast ($<$ 1 d) at high temperatures (around 1800–2400 K). This makes Al_2O_3 the favoured candidate to become the first dust particles in the inner AGB wind. The second favoured candidates are MgO-clusters, which can form fast ($<$ 1 d) around 1500 K. We find, that $(MgO)_9$ forms more easily than the largest considered cluster $(MgO)_{10}$ thanks to its higher stability. This is a consequence of the used non-classical nucleation description that relies on the GFE of the clusters, which is lower for $(MgO)_9$ than for $(MgO)_{10}$, making the former more energetically stable. Another consequence of the non-classical description is the preferred cluster sizes $N = 2$, 4, 6, and 9, a situation that would never occur when using a classical nucleation theory (also noted by Köhler et al. 1997). The third preferred dust candidates are TiO_2-clusters, which only form below 1000 K at a relatively slow rate (time-scale of tens of days compared to hours for MgO- and Al_2O_3-clusters). Finally, we discard SiO-clusters to be important as first dust species as their growth requires conditions that are too cold and too dense compared to the conditions in an inner AGB wind. SiO-clusters might form dust grains further out in the wind, where the temperature is below 500 K.

Using the MN or PN description can result in substantial differences in typical formation times of the nucleation products, hence in their abundances after 1 yr (Figs 2 and 3). The most striking difference is the absence of large clusters at low temperatures when using the MN description. This can have profound implications while the wind is cooling down, underestimating the total number of large clusters. Using the abundance of the largest clusters as a gauge of dust formation, the MN description will yield less dust, which can delay or even hamper wind driving. The formation time of large clusters can be several times larger when using the MN description. For example, the convergence of $(TiO_2)_{10}$ takes 60 d as compared to less than 20 d when using the PN description. For $(MgO)_9$ the difference is 180 d compared to a few hours (Fig. 3). Additionally, at our benchmark density of 10^{-9} kg m^{-3} the abundance of $(MgO)_9$ converges to roughly 10^{12} m^{-3} in mere hours in the polymer case whereas in the monomer case it takes almost 200 d to converges to only 10^{10} m^{-3} (Fig. 3).

Although the abundance of some clusters converges, this does not happen for all clusters over the entire temperature regime. This result implies that no all clusters have reached equilibrium abundances yet. Hence, the assumption of a steady-state nucleation is generally not valid in the entire temperature range. Therefore, it is necessary to use a time-dependent nucleation description to accurately trace the nucleation process.

5.2 Comprehensive chemical nucleation network

Although Al_2O_3-clusters are the primary dust precursor candidate according to the closed nucleation models (Section 5.1), no Al_2O_3-clusters form in the comprehensive nucleation models since the smallest building block, the monomer, cannot be created. Most Al remains atomic, though up to maximally 1 per cent can form molecules [AlO, AlH, $Al(OH)_2$, and $Al(OH)_3$, Fig. 5]. The second favoured candidates, MgO-clusters, do not exist either because all the available Mg remains atomic. The third favoured candidates according to the closed nucleation model, TiO_2-clusters, form equally efficient in the comprehensive nucleation model. Lastly, as in the closed nucleation models, SiO-clusters are discarded as first dust precursors in the considered temperature–density regime.

These results suggest that, of the considered candidates, TiO_2-clusters are the only possible dust precursors. However, first there is ample evidence that presolar AGB grains mainly encompass Al_2O_3-grains rather than TiO_2-grains (Hutcheon et al. 1994; Nittler et al. 1994; Choi et al. 1998; Nittler et al. 2008; Bose et al. 2010b). Secondly, dust has been observed to exist close to AGB stars, at $\sim 1.5R_\star$ for R Dor (Khouri et al. 2016), at $<2R_\star$ for R Dor, W Hya, and R Leo (Norris et al. 2012), and at $<2R_\star$ for W Hya (Zhao-Geisler et al. 2015; Ohnaka, Weigelt & Hofmann 2016). The temperature corresponding to those spatial regions is roughly 1500–2000 K, which is higher than the formation temperature

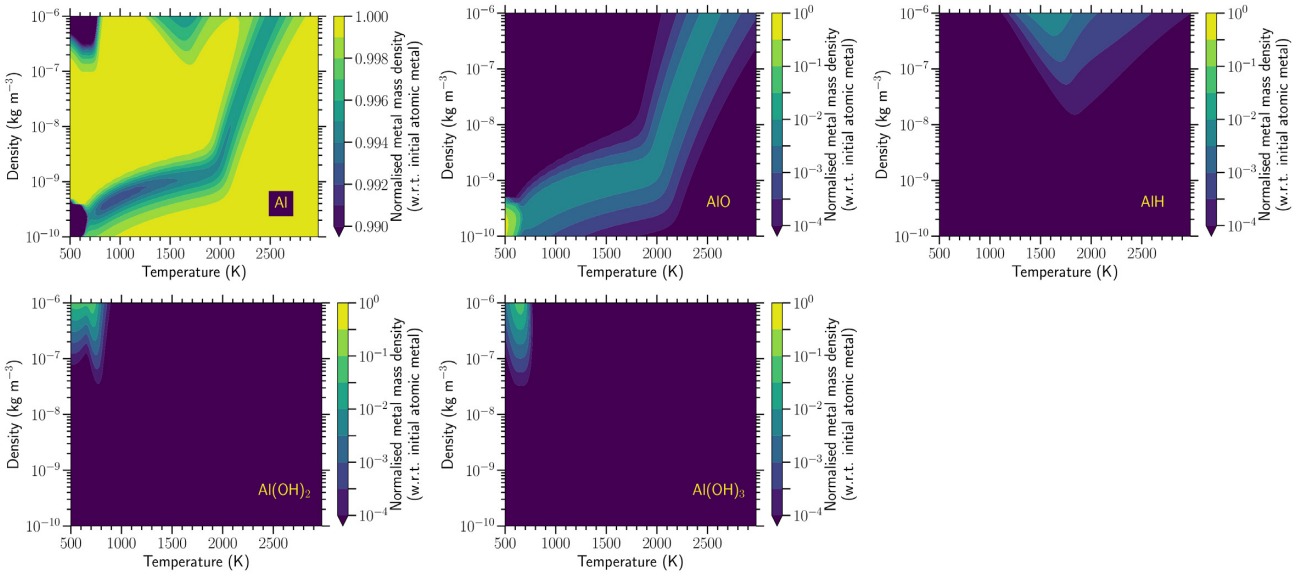

Figure 5. Normalized mass density after 1 yr of the most abundant Al-bearing molecules for the comprehensive chemical nucleation models using the PN description. Most Al remains atomic with up to 1 per cent in Al-bearing molecules. Al_2O_3, nor its precursors Al_2O_2, AlO_2 are able to form anywhere in the considered (T, ρ)-grid. Hence, no Al_2O_3-clusters can form either. We believe this issue is due to incomplete rate coefficients of Al-molecule formation reactions. An overview of all Al-bearing molecules plus a temporal evolution of Al and AlO can be found in Appendix D2 with an in-depth analysis in Sections 4.2 and 5.2.

of $(TiO_2)_{10}$, that is around 1000–1200 K (Figs 2 and 4). Large MgO and Al_2O_3-clusters, however, are able to form at such high temperatures (Fig. 2). Both observational arguments question the viability of TiO_2-clusters as first dust species and favour Al_2O_3-clusters, yet our comprehensive model does not predict this. This discrepancy indicates that our current model lacks chemical reaction physics to form Al_2O_3 monomers. Since we cannot form any of the two Al_2O_3 precursors either (Al_2O_2 and AlO_2, Table 2), we believe that the current reaction rate coefficients involving Al-oxides are incorrect and need revision or that alternative small Al_2O_3-cluster formation pathways are missing.

Table 2. Formation of Al_2O_3 can only occur via Al_2O_2 or AlO_2, according to the reactions available in the literature. M is by convention a third body that can be any chemical species.

[a] $AlO + AlO + M \rightarrow Al_2O_2 + M$	
[a] $Al + AlO_2 + M \rightarrow Al_2O_2 + M$	
[a] $Al_2O + O + M \rightarrow Al_2O_2 + M$	[a] $Al_2O_2 + O + M \rightarrow Al_2O_3 + M$
[b] $AlO + O + M \rightarrow AlO_2 + M$	[a] $AlO_2 + AlO + M \rightarrow Al_2O_3 + M$
[b] $AlO + O_2 \rightarrow AlO_2 + O$	
[a] $AlO + CO_2 \rightarrow AlO_2 + CO$	

Note. Rate coefficients are determined by: [a]Reversed of Catoire, Legendre & Giraud (2003) and Washburn et al. (2008) via detailed balance. [b]Sharipov et al. (2012).

6 DISCUSSION

This section discusses the limitations of our models (Section 6.1) and compares our model results with other literature studies (Section 6.2).

6.1 Limitations

This section focuses on the limitations of the improved nucleation theory (Section 6.1.1), the used chemical reactions (Section 6.1.2), and the inference of dust properties (Section 6.1.3).

6.1.1 Nucleation theory

Our non-classical, non-equilibrium nucleation theory has some limitations. The most prominent one is most likely that it describes the growth of clusters as an inelastic collision between rigid spheres. This assumption does not account for the shape of the clusters nor mutual interaction forces. Using detailed chemical reaction coefficients for each cluster reaction, which account for possible energy barriers, would be a large improvement. Unfortunately, such information does not yet exist. Recently, Sharipov & Loukhovitski (2018) have calculated rate coefficients of the dimerization of Al_2O_3 based on Rice–Ramsperger–Kassel–Marcus (RRKM) theory, which is a more realistic approximation than the using the rigid spheres. We show both approximations as an example on how much the coefficients can differ (Fig. 6). Similarly, Suh, Zachariah & Girshick (2001) and Bromley et al. (2016) have determined SiO-clustering rate coefficients with RRMK theory.

Additionally, in the cluster growth coefficient (equation 11), we write the radius of each cluster as a function of the monomer radius. However, since we know the shape of each cluster, it is possible to calculate an effective radius for each cluster, yielding a more correct geometrical cross-section between cluster collisions. Another limitation is set by using spontaneous clusters destruction reactions that rely on detailed balance. Incorporating chemical or collisionally induced destruction reactions would increase the accuracy of the model. Furthermore, the entire nucleation process is assumed to be homomolecular. There is, however, no good reason that it cannot be heteromolecular. Heteromolecular nucleation is most likely necessary to create $MgAl_2O_4$-clusters, which are abundant in presolar AGB grains, or Mg-containing silicates (Goumans & Bromley 2012). Including heteromolecular nucleation will increase the number of possible reactions exponentially and will increases the amount of detailed quantum mechanical calculation and data needed for those reaction rate coefficients.

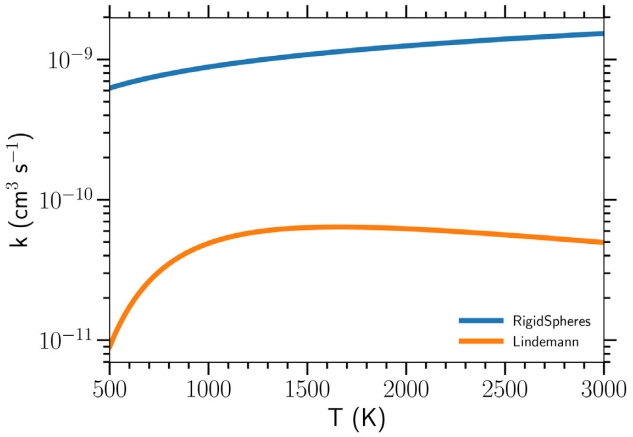

Figure 6. The reaction rate coefficients of $Al_2O_3 + Al_2O_3 \rightarrow (Al_2O_3)_2$ with the approximation of a collision of rigid spheres, used in this work, and calculated with RRMK theory plus a Lindemann fit by Sharipov & Loukhovitski (2018). As this latter also depends on the total number density, we have chosen a typical value for the inner AGB wind, $n_{tot} = 10^{18}$ m^{-3}. Our approximation over predicts the dimerization by roughly an order of magnitude compared to the more realistic coefficient using the Lindemann fit. Therefore, using a rigid sphere approximation, as in this work, will most likely overestimate the efficiency of the nucleation process.

The assumption that nucleation starts with the formation of the monomer is not yet established. Small clusters might be formed via pathways that bypass the monomer molecule. This could possibly solve the issue of not forming Al_2O_3-monomer in our models. Additionally, the fact that nucleation occurs via the addition of monomer-multiples with a fixed stoichiometry is not established either. Clusters could possibly grow via the addition of other stoichiometric ratios, as investigated by Patzer et al. (2005) for small aluminium oxide clusters.

Note that the used nucleation description considers the process as a statistical ensemble of particles that all have the same mean temperature. However, as this is a process of molecular interactions, the notion of 'temperature' can become unclear. In reality, the particles have a temperature distribution around a mean kinetic temperature. Molecular dynamics simulations, which do not rely on a mean temperature, reveal that small temperature fluctuations amongst particles initiate the nucleation process (Tanaka et al. 2011; Diemand et al. 2013; Toxvaerd 2015).

A last limitation is the artificial maximum cluster size. In reality, the clusters would continue to grow to form solid material. This material can then, on its turn, sublimate and return nucleation species to the gas phase. Whether the sublimation process returns small clusters, monomers, atoms, or simple molecules is unclear. Additionally, to estimate the sublimation rate one needs the binding energies of the surface layer of the solid material. However, the phase transition process to a solid dust grain is often described by one fast reaction (e.g. Huang et al. 2009; Bojko, DesJardin & Washburn 2014). A better approach would be to evolve the nucleation of clusters until a chosen maximal cluster size is reached, after which it can be considered as a solid particle and can grow via grain–grain interactions such a coagulation.

6.1.2 Chemical reactions

To infer abundances of the largest nucleation clusters, it is crucial to correctly predict the creation of its fundamental building block, the monomer. Hence, the chemical reaction path ways from atoms to monomers have to be accurate. However, astrochemical data bases lack the necessary monomer formation reactions. Yet, there are individual studies that provide some reactions, but they are scarce depending on the nucleation candidate. To determine the AGB dust precursors, we believe that Ti and Al reactions are the most pressing. There are hardly any Ti-related reactions (Appendix E) and most Al-related reactions have extremely high reaction barriers. The latter mainly originate from combustion studies and are therefore often only determined in the high-density limit. Moreover, most Al-related reaction rate coefficients are determined from destruction of larger molecules, which is the opposite of what is actually needed. Therefore, the growth coefficients rely on the assumption of detailed balance.

It is important that the entire chemical network contains sufficient reactions with accurate rates. As pointed out by Boulangier et al. (2019), we are largely dependent on the astrochemical data bases that do not contain all the reactions that are necessary. Due to the lack of reactions rate coefficients and especially the unknown temperature dependence, caution is advised when interpreting chemical evolution results and the existence of certain molecules based on the gas temperature.

6.1.3 Inference of dust properties from clusters

This work focuses on nucleation clusters to infer AGB dust properties such as abundance, composition, and formation times. However, the largest clusters that we consider are only a fraction of the size of a dust grain nor do they resemble the bulk geometry. The largest clusters' radii range from 0.16 to 0.71 nm whereas dust grains can be as large as a few micron. Lamiel-Garcia et al. (2017) predict that TiO_2-clusters only resemble the bulk geometry from $N \geq 125$. For highly ionically bonded materials such as MgO-clusters this can already be at $N = 20$ due to the strong electrostatic interactions between atoms. Therefore, one has to be careful when using nucleation clusters as a gauge for dust grains. Yet, due to computational constraints a small cross-over size, from clusters to dust, has to be chosen. From this cross-over size, the particles should not be considered as molecular clusters any more but as tiny grains that can numerically be binned in size and can grow via various physical processes (e.g. Jacobson 2013; Grassi et al. 2017; McKinnon et al. 2018; Sluder et al. 2018). Because of our artificial maximum cluster size, one has to be cautious when interpreting the abundances of the largest clusters in this work since in reality these will most likely continue to grow to actual dust grains.

6.2 Comparison with literature

This section compares our model results with other nucleation models (Section 6.2.1), with seed particle requirements of dynamical wind models (Section 6.2.2), and with molecular observations of AGB stars (Section 6.2.3).

6.2.1 Nucleation models

In contrast to Gobrecht et al. (2016), our most complete model (comprehensive network with PN) does not produce any Al_2O_3-clusters. However, unlike this work, Gobrecht et al. (2016) used a simplified formulation to determine reversed formation rates for Al-bearing molecules resulting in a temperature independent rate coefficients. Some key formation reactions reveal that the used rate coefficients can differ by up to 10 orders of magnitude [e.g. AlO + AlO + M $\rightarrow$ Al_2O_2 + M, Fig. 7. Note that Sluder et al. (2018) use an

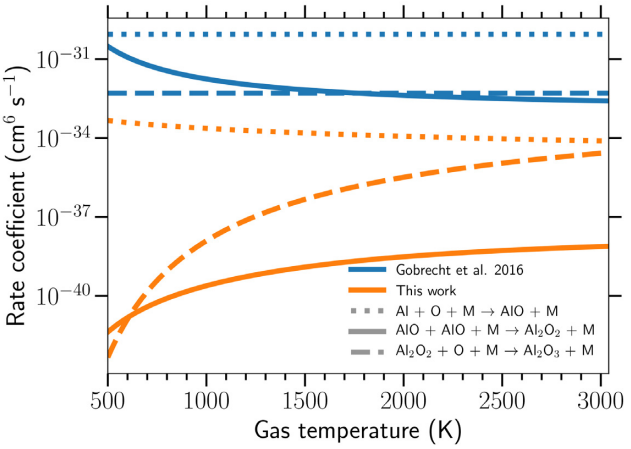

Figure 7. The reaction rate coefficients of some key Al_2O_3 formation reaction used by Gobrecht et al. (2016) are 2–10 orders of magnitude higher than the ones used is this work. These large differences could explain why Gobrecht et al. (2016) form Al_2O_3 and we do not. Moreover, they estimate the barrierless three-body reactions of the type A + B + M → AB + M to be temperature independent, hampering an investigating of the temperature dependence for Al_2O_3-cluster formation.

even higher rate coefficient for this reaction.]. Such large differences could explain different results of Gobrecht et al. (2016), as compared to this work. Moreover, we give a more realistic rate description by incorporating a temperature dependence in addition to the strong density dependence that is crucial to investigate the existence of large clusters and dust grain as a function of temperature (e.g. Al_2O_2 + O + M → Al_2O_3 + M, Fig. 7). Compared to observations, Gobrecht et al. (2016) overpredict the abundance of Al-bearing molecules (AlO and AlOH), whereas our models agree better with the most recent observations (Section 6.2.3).

An approach similar to this work has recently been used by Savel'ev & Starik (2018), who investigated the nucleation of Al_2O_3-clusters up to a cluster size of 75 during the combustion of aluminized fuels. Similarly, they also model the nucleation kinetically with a set a chemical reactions. Their nucleation reactions, however, only consider monomer interactions. They do consider much larger clusters than we do. However, the authors rely on estimates (interpolations) of the GFEs for $N = 5-75$ and do not perform DFT calculations of the global minima candidates. The authors do not provide the geometries of these larger sized Al_2O_3-clusters. Therefore, we cannot verify these isomers with the lowest energy structures used in the present study. Moreover, it is difficult to compare results since their environment has a density of several orders of magnitude higher making the nucleation occur on milli- and microsecond time-scales. See Starik, Savel'ev & Titova (2015) for a recent review of modelling aluminium nanoparticles in the fuel combustion community.

The nucleation efficiency of species is often determined by the steady-state nucleation rate, J_*/n_H, which represents the number of dust seed particles formed per second per total number of hydrogen. However, this rate relies on two main assumptions. First, growth of clusters only occurs via addition of monomers. Secondly, the system of clusters is in a steady state, i.e. the number densities of all clusters remain constant over time, ergo chemical equilibrium. This latter implies that the net formation of all clusters is the same and size independent. Detailed derivations for the steady-state nucleation rate can be found in Patzer, Gauger & Sedlmayr (1998) but the notation used by Bromley et al. (2016) is clearer. The latter explicitly shows that J_*/n_H solely depends on the amount of monomers[21] and all rate coefficients between clusters. To determine this equilibrium abundance, one has to know the GFE of the lowest energy configuration for all cluster sizes (equation 17). This data is unavailable for large clusters. It is often unclear how this abundance is determined in nucleation papers, either from the vapour pressure of the monomer and the solid form (as explained by Patzer et al. 1998; Helling & Woitke 2006)[22] or by chemical equilibrium calculations of the gas without considering the clusters (e.g. Jeong et al. 2003; Lee et al. 2015).[23] Because the steady-state MN description differs significantly from ours and requires knowing the equilibrium abundance of the monomer, it is difficult to compare with. Using J_*/n_H, it is often claimed that only TiO_2 nucleates efficiently enough to form the first dust precursor. We limit the comparison to our MN description since the steady-state one also assumes nucleation by monomers. When comparing our results with Jeong et al. (2003, fig. 1), we note that both predictions of $(TiO_2)_2$-clusters have a steep cut-off around 1000 K (Fig. 2). However, our time-dependent description does not yield the high nucleation that the steady-state one does at low temperatures since the availability of monomers decreases quickly hereby quenching the growth process. Additionally, the assumption of steady state is invalid since there is a clear time dependence in cluster growth (Fig. 3). Jeong et al. (2003) exclude Al_2O_3-clusters to be a primary dust precursor due to the low J_*/n_H. One should be careful with interpreting this result since, as they point out, this is due to the low equilibrium abundance of the monomer and not necessarily the capability of nucleating Al_2O_3-clusters. They do not discuss the efficiency of Al_2O_3 versus TiO_2-nucleation based on stability of the clusters. We find that, if Al_2O_3-monomers could exist, they will nucleate at much higher temperatures than TiO_2 (Fig. 2). However, we are also unable to form the Al_2O_3-monomers with an initial atomic gas (Section 4.2.4).

Our results indicate that Al_2O_3-nucleation is dominant at high temperatures but the formation of the monomer via chemical reactions is unattainable with currently available data. Moreover, there is experimental evidence that small Al_2O_3-clusters do exist when vaporizing the solid material (van Heijnsbergen et al. 2003; Demyk et al. 2004; Sierka et al. 2007) This is a clear incentive for the scientific community to investigate rate coefficients of Al-bearing reactions at high temperatures. Without this data, it will remain unclear which species forms the first dust precursors in AGB winds.

6.2.2 *Dynamical models*

Höfner et al. (2016) show that the minimal normalized number of Al_2O_3 dust seed particles (assumed to be clusters of size $N = 1000$) for driving an AGB wind is of the order of $n_s/n_H \sim 10^{-16}$, with n_s the seed particle number density. For comparison, we

[21] Since a steady state is assumed, this refers to the number of monomers at chemical equilibrium. A detail that is usually overlooked.

[22] Determining the equilibrium monomer abundance from the phase equilibrium with the bulk material via the vaporization pressure inherently assumes that the bulk material exists. However, since we are investigating the existence of bulk material can actually happen in certain conditions, such assumption should not be made.

[23] Though we could not confirm which of these two methods Jeong et al. (2003) used, we note that if the vapour pressure was used than the nucleation of Al_2O_3 should be higher than that of TiO_2 since the former has a lower vapour pressure. According to that method, this means less monomers thus all material is in the solid form. However, they find a smaller J_*/n_H for Al_2O_3 than for TiO_2.

do a rough extrapolation of our results by assuming that all the largest Al_2O_3-clusters get turned into clusters of size $N = 1000$. This is in line with rapid formation of the largest clusters and depletion of the smallest ones (Section 4.1.4). Since our largest cluster has roughly size $N = 10$, the number of seed particles of $N = 1000$ would be 100 times smaller. If we compare with Al_2O_3-clusters and assume that 1 per cent of the available Al turns into Al_2O_3 (Section 4.2.4 and 5.2), then the total number of largest clusters is roughly 10 per cent of the initial number of monomers. This translates to $n_{(Al_2O_3)_{1000}}/n_{Al} \approx 10^{-5}$. Using n_{Al}/n_H from Table 1, this yields a normalized number of seed particles $n_{(Al_2O_3)_{1000}}/n_H \approx 3 \times 10^{-11}$, which is already 100 000 times more than needed according to the models of Höfner et al. (2016). We can also compare this with the number of $(TiO_2)_{10}$-clusters. Here, no assumption on the number of monomers has to be made because the comprehensive network model with PN already predicts the amount of $(TiO_2)_{10}$. This is roughly 10 per cent of the available number of Ti. Again assuming that the number of $(TiO_2)_{1000}$-clusters is 100 times smaller than $(TiO_2)_{10}$ and using the initial n_{Ti}/n_H from Table 1, yields $n_{(TiO_2)_{1000}}/n_H \approx 8 \times 10^{-11}$. This is in line with the $(Al_2O_3)_{1000}$-cluster extrapolation.

6.2.3 *Observations*

Our prediction of TiO_2-clusters (Fig. 4) agrees with Kamiński et al. (2017), who state that there is no solid TiO_2 close to the star ($T > 1000$ K). They also claim that TiO and TiO_2 are abundantly present in the extended envelope (170–500 K) and therefore TiO_2-clusters should not significantly exist to aid in wind driving. However, according to models of Höfner et al. (2016), a tiny fraction of seed particles ($n_s/n_H \sim 10^{-16}$) can be sufficient to aid in wind driving (Section 6.2.2). The lower left corner of our (T, ρ)-grid most closely resembles the extended envelope regime (i.e. cold and sparse), which shows that the TiO_2 molecule and TiO_2-clusters can simultaneously be present (Fig. D22). When intuitively extrapolating to lower temperatures and lower densities, as if moving further out into the extended envelope, we expect a higher TiO_2 and TiO abundance and less TiO_2-clusters.

Khouri et al. (2018) observe that for the oxygen-rich AGB star o Cet 4.5 per cent of the atomic Ti is locked-up in TiO_2. It is, however, difficult to compare with our model grid since the presence of the molecule is extremely sensitive to gas temperature and its abundance ranges from 0 to 100 per cent of the intitial atomic Ti (Fig. D22). As it is unclear what the temperature coverage of the observation is, the derived abundance is most likely an average in a certain temperature range. Kamiński et al. (2016) discovered AlO, AlOH, and AlH in o Cet but could only determine the abundance of AlO. They find $n_{AlO}/n_H = 10^{-9}$–10^{-7}, which agrees with our model predictions that maximally 1 per cent of all Al is turned into molecules, with AlO the most abundant molecule $\sim n_{AlO}/n_H < 10^{-8}$. Kamiński et al. (2016) do state that AlOH is present in a gas temperature of 1960 ± 170 K, and that AlH is detected between 2.5 to 4 $R_\star$. Both observational constraints comply with our model predictions (Fig. D25). Additionally, Decin et al. (2017) find that for AGB stars IK Tau and R Dor the amount of AlO, AlOH, and AlCl accounts for maximally 2 per cent of the total aluminium budget. Both observations are in line with our prediction that maximally 1 per cent of all Al is turned into molecules (Fig. 5). The amount of detected AlOH in R Dor only accounts for roughly 0.02 per cent, yet this is still significantly more than our models predict (Fig. D25). Lastly, Khouri et al. (2018) also deduce that

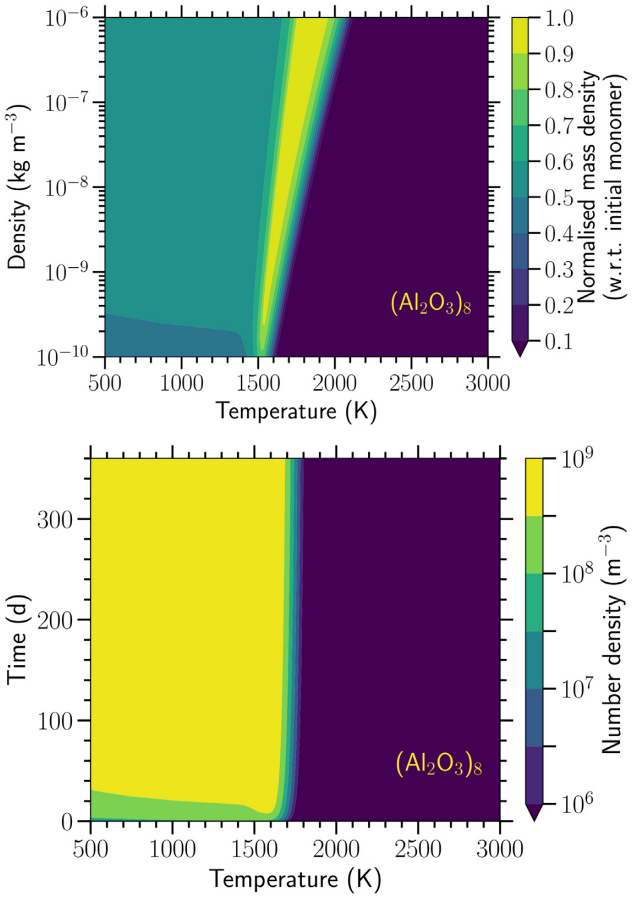

Figure 8. Normalized mass density after 1 yr (top) and temporal evolution of the absolute number density at the benchmark total gas density $\rho = 1 \times 10^{-9}$ kg m^{-3} (bottom) of $(Al_2O_3)_8$ for the closed nucleation model with an initial Al_2O_3 abundance of 1 per cent of the available Al using the PN description. The results are similar to the closed nucleation model with all Al turned into Al_2O_3 (Figs 2 and 3). Due to the lower amount of species the formation threshold is slightly lower at 1600–2100 K and convergence takes a little longer, roughly 20 d.

less than 0.1 per cent of the atomic Al is converted into AlO. In conclusion, all three observational studies agree with our prediction that maximally 1 per cent of all Al is turned into molecules. Our prediction also better supports the recent observations than the significantly higher abundances of Al-bearing molecules predicted by models of Gobrecht et al. (2016).

As both observations and our comprehensive model agree that maximally 1 per cent of all atomic Al turns into a molecule (Section 4.2.4), it is interesting to analyse the results of a closed nucleation model with only 1 per cent of the available Al as initial Al_2O_3 abundance. We choose to only use the PN description. Compared to a 100 per cent initial abundance, the temperature formation threshold of $(Al_2O_3)_8$ has slightly lowered to 1600–2100 K (Fig. 8). This is expected as a lower density produces less collisions therefore making it more difficult to form clusters at higher temperatures. Similarly, $(Al_2O_3)_8$ converges only after roughly 20 d that is significantly longer than the 5–10 h for the 100 per cent initial abundance model (Fig. 8). Besides the temporal effects, the results are analogous to the 100 per cent case where $(Al_2O_3)_8$ also contains more than 90 per cent of the available monomers at the highest formation temperatures.

7 SUMMARY AND PROSPECTS

In this paper, we have constructed and investigated an improved nucleation theory by abandoning the assumption of chemical equilibrium, dropping the restriction of cluster growth by only monomers, and using accurate quantum mechanical properties of molecular clusters. We have examined the viability of TiO_2, MgO, SiO, and Al_2O_3 as candidates of the first dust precursors in oxygen-rich AGB winds. The choice of candidates is based on rigorous theoretical and observational evidence (Section 3.2).

This work consists of two main nucleation descriptions, one that only allows cluster growth via monomers and one that allows polymer interaction. Both assume the nucleation processes to be homogeneous and homomolecular. With these descriptions, two main types of systems are evolved in a grid of temperature and density that is typical for AGB winds: a closed nucleation system and a comprehensive chemical nucleation system. The former considers the growth of one nucleation candidate species with the monomer as the smallest building block and assumes that all available atomic metal is locked-up in the monomer. The latter allows chemical interaction between species in a gas mixture that includes all nucleation species and starts with an atomic composition. The former provides insight in the nucleating efficiency of each candidate in temperature and density space, and the latter yields a more complete chemical nucleation model by removing the assumption of the a priori existence of the monomer (Section 3).

Constructing the nucleation reaction networks required quantum mechanical data of all clusters, which we calculated with high precision DFT. Since such calculations exponentially increase with cluster size, we limit the maximal size to roughly $N = 10$. The comprehensive chemical reaction network is constructed by adding relevant chemical reactions to an already carefully designed reduced network for AGB winds (Boulangier et al. 2019). The extension includes all relevant and available reactions to form the nucleation monomers. Since a significant amount of reversed reactions is not present in the literature, quantum mechanical data for the participating species is needed to calculate those reaction rate coefficients. We have gathered as much as possible data from the literature and performed DFT calculations when this was unavailable (Section 3.6).

Overall, using the MN description as compared to the polymer one, will underestimate the abundance and overestimate the formation time of the large clusters. Using the abundance of the largest clusters as a gauge of dust formation, the MN scenario would underestimate the amount of dust and overestimate its formation time. This can lead to less efficient wind driving or even the absence of a wind in theoretical simulations. The monomer description also inhibits the formation of large clusters at low temperatures due to a rapidly developing lack of monomers, which by design is the only growth mechanism. The polymer description does not suffer from this limitation and is therefore more realistic. Comparison with equilibrium abundance ratios reveals that the assumption of equilibrium is not valid over the entire temperature range for a period of 1 yr. Hence, a time-dependent description in necessary to investigate the nucleation process in AGB winds.

The closed nucleation models, which assume that the nucleation monomers are present, predict that Al_2O_3 is the primary candidate to be the first AGB dust precursor. These clusters rapidly form at much higher temperatures than any other cluster, around 1800–2400 K and in less than a few days. Rapid dust formation at high temperatures will aid in driving the AGB wind, since the wind is cooling down from hot shocks (∼10 000 K, Boulangier et al. 2019). At around 1500–1700 K, large MgO-clusters can form and only at 1000–1200 K large TiO_2-clusters arise. Formation of SiO-clusters is not favourable in the considered temperature range but requires colder conditions. Note that the above conclusions are drawn on the underlying assumption that the monomer exists (Section 4.1).

The comprehensive chemical nucleation model yields different results from the closed nucleation ones. First, it does not predict any Al_2O_3-clusters, nor its monomer, nor its molecular precursors (Al_2O_2 and AlO_2) but most Al remains atomic with maximally 1 per cent in Al-bearing molecules, which is mainly AlO. Secondly, all available Mg remains atomic and no MgO-clusters can exist. Hence, the most favoured nucleation candidates, according to the closed models, are non-existent. Only TiO_2-clusters exist in the comprehensive model, with similar formation conditions as in the closed model. SiO-clusters are again discarded due to their low formation temperature (Section 4.2).

The results from the comprehensive nucleation model suggest that TiO_2 is the only possible AGB dust precursor of the considered nucleation candidates. However, this contradicts the substantial amount of Al_2O_3-favouring evidence. First, the number of Al_2O_3-clusters found in presolar AGB grains far exceeds the amount of TiO_2-clusters. Secondly, numerous AGB dust observations indicate that dust already exists close to the star and thus at temperatures as high as 1500 to 2000 K, a regime in which, according to our model results, only Al_2O_3-clusters can exist. TiO_2-clusters require temperatures below 1000–1200 K. We believe that this discrepancy suggests that our current chemical reaction network is incomplete. Additionally, since there is experimental evidence that gaseous small Al_2O_3-clusters can exists, we believe that either the current reaction rate coefficients involving AlO-bearing molecules are not accurate enough and need to be re-evaluated, or that alternative small Al_2O_3-cluster formation pathways are missing. Moreover, most Al-molecule formation rate coefficients are unavailable in the literature and rely on the assumption of detailed balance with their corresponding destruction process. We therefore urge the scientific community to investigate rate coefficients of formation reactions of Al-bearing molecules at high temperatures. Without this data, it will remain unclear which species will form the initial dust precursors in AGB winds.

This paper has constructed and investigated an improved nucleation theory for more accurate modelling of the formation of dust. The improved description is time-dependent, allows growth by polymers, and considers quantum mechanical molecular properties. This procedure is universal and can be applied to any astrophysical environment, where this paper focuses on AGB winds. This work serves as a initial model that will be extended with macroscopic dust formation processes such as gas accretion, gas sputtering, dust coagulation, dust shattering, and dust evaporation in a future paper. It is the second in a series where we strive for increased self-consistency regarding chemistry, dust creation, and dynamics. The developed and improved chemical nucleation description can be incorporated into a hydrochemical model such as the first paper in this series (Boulangier et al. 2019). Currently, the results indicate which species, how much, how fast, and under which conditions they nucleate in an AGB wind.

ACKNOWLEDGEMENTS

JB, DG, and LD acknowledge support from the ERC consolidator grant 646758 AEROSOL. This research made use of MATPLOTLIB (Hunter 2007), NUMPY (Oliphant 2006), and ASTROPY (Robitaille et al. 2013; The Astropy Collaboration 2018), which are community-developed core PYTHON packages for science and astronomy.

REFERENCES

Abel T., Anninos P., Zhang Y., Norman M. L., 1997, New Astron., 2, 181
Archibong E. F., St-Amant A., 1999, J. Phys. Chem. A, 103, 1109
Asplund M., Grevesse N., Sauval A. J., Scott P., 2009, ARA&A, 47, 481
Atkinson R. et al., 2004, Atmos. Chem. Phys., 4, 1461
Bauschlicher C. W., Schwenke D. W., 2017, Chem. Phys. Lett., 683, 62
Becke A. D., 1993, J. Chem. Phys., 98, 1372
Becker K., Fink E., Leiss A., Schurath U., 1978, Chem. Phys. Lett., 54, 191
Beckmann A., Böklen K. D., Bremer G., Elke D., 1975, Z. Phys. A, 272, 143
Bojko B. T., DesJardin P. E., Washburn E. B., 2014, Combust. Flame, 161, 3211
Bose M., Floss C., Stadermann F. J., Stroud R. M., Speck A. K., 2010a, in Lunar Planet. Sci. Conf. p. 1812
Bose M., Floss C., Stadermann F. J., 2010b, ApJ, 714, 1624
Bose M., Floss C., Stadermann F. J., Stroud R. M., Speck A. K., 2012, Geochim. Cosmochim. Acta, 93, 77
Boulangier J., Clementel N., van Marle A. J., Decin L., de Koter A., 2019, MNRAS, 482, 5052
Bromley S. T., Gómez Martín J. C., Plane J. M. C., 2016, Phys. Chem. Chem. Phys., 18, 26913
Burcat A., Ruscic B., 2005, Technical Report, Third Millennium Ideal Gas and Condensed Phase Thermochemical Database for Combustion (with update from active thermochemical tables). Argonne National Laboratory (ANL), Argonne, IL, http://www.osti.gov/servlets/purl/925269-199FKl/
Campbell M. L., McClean R. E., 1993, J. Phys. Chem., 97, 7942
Capitelli M., Coppola C. M., Diomede P., Longo S., 2007, A&A, 470, 811
Catoire L., Legendre J.-F., Giraud M., 2003, J. Propul. Power, 19, 196
Chase M. W. J., 1998, Phys. Chem. Ref. Data, 9
Chen M., Felmy A. R., Dixon D. A., 2014, J. Phys. Chem. A, 118, 3136
Choi B. G., Huss G. R., Wasserburg G. J., Gallino R., 1998, Science, 282, 1284
Clouet E., 2009, in Furrer D., Semiatin S., eds, ASM Handbook, Vol. 22A, Fundamentals of Modeling Metals Processing. ASM International, Novelty (USA), p. 203, https://arxiv.org/pdf/1001.4131v2.pdf
Corà F., 2005, Mol. Phys., 103, 2483
Decin L. et al., 2017, A&A, 608, 55
Decin L., Danilovich T., Gobrecht D., Plane J. M. C., Richards A. M. S., Gottlieb C. A., Lee K. L. K., 2018, ApJ, 855, 113
Dell'Agli F., García-Hernández D. A., Schneider R., Ventura P., La Franca F., Valiante R., Marini E., Di Criscienzo M., 2017, MNRAS, 467, 4431
DeMore W. et al., 1997, JPL Publ., 97-4, 226
Demyk K., van Heijnsbergen D., von Helden G., Meijer G., 2004, A&A, 420, 547
Depew K., Speck A., Dijkstra C., 2006, ApJ, 640, 971
Diemand J., Angélil R., Tanaka K. K., Tanaka H., 2013, J. Chem. Phys., 139, 074309
Farrow M. R., Chow Y., Woodley S. M., 2014, Phys. Chem. Chem. Phys., 16, 21119
Ferrarotti A. S., Gail H.-P., 2006, A&A, 447, 553
Forrey R. C., 2013, ApJ, 773, L25
Frisch M. J. et al., 2013, Gaussian 09, Revision E.01, http://Gaussian.com/
Furtenbacher T., Szidarovszky T., Hrubý J., Kyuberis A. A., Zobov N. F., Polyansky O. L., Tennyson J., Császár A. G., 2016, J. Phys. Chem. Ref. Data, 45, 043104
Gail H.-P., Sedlmayr E., 1988, A&A, 206, 153
Gail H.-P., Sedlmayr E., 1999, A&A, 347, 594
Gamache R. R. et al., 2017, J. Q. Spectrosc. Radiat. Transfer, 203, 70
Glover S. C., Abel T., 2008, MNRAS, 388, 1627
Glover S. C., Federrath C., Low M. M., Klessen R. S., 2010, MNRAS, 404, 2
Gobrecht D., Cherchneff I., Sarangi A., Plane J. M. C., Bromley S. T., 2016, A&A, 585, A6
Gobrecht D., Cristallo S., Piersanti L., Bromley S. T., 2017, ApJ, 840, 117
Gobrecht D., Decin L., Cristallo S., Bromley S. T., 2018, Chem. Phys. Lett., 711, 138
Gordon I. et al., 2017, J. Q. Spectrosc. Radiat. Transfer, 203, 3
Goumans T. P. M., Bromley S. T., 2012, MNRAS, 420, 3344
Grassi T., Bovino S., Schleicher D. R., Prieto J., Seifried D., Simoncini E., Gianturco F. A., 2014, MNRAS, 439, 2386
Grassi T., Bovino S., Haugbølle T., Schleicher D. R. G., 2017, MNRAS, 466, 1259
Habing H., Olofsson H., 2004, Asymptotic Giant Branch Stars, Springer, Berlin
Haris K., Kramida A., 2017, ApJS, 233, 16
Helling C., Winters J. M., 2001, A&A, 366, 229
Helling C., Woitke P., 2006, A&A, 455, 325
Herzberg G., 1966, Molecular Spectra and Molecular Structure. Vol. 3: Electronic Spectra and Electronic Structure of Polyatomic Molecules. Van Nostrand Reinhold Company, New York
Higuchi Y., Fukuda Y., Fujita Y., Yamakita N., Imajo T., 2008, Chem. Phys. Lett., 452, 245
Höfner S., Bladh S., Aringer B., Ahuja R., 2016, A&A, 594, A108
Huang Y., Risha G. A., Yang V., Yetter R. A., 2009, Combust. Flame, 156, 5
Huber K. P., Herzberg G., 1979, in Mol. Spectra Mol. Struct. Van Nostrand Reinhold Company, New York, p. 8
Hunter J. D., 2007, Comput. Sci. Eng., 9, 90
Hutcheon I. D., Huss G. R., Fahey A. J., Wasserburg G. J., 1994, ApJ, 425, L97
Hynes K. M., Gyngard F., 2009, Technical Report, The Presolar Grain Database. Laboratory for Space Sciences and Department of Physics, Washington University (USA), http://presolar.wustl.edu/ pgd
Jacobson M. Z., 2013, Fundamentals of Atmospheric Modeling, 2nd edn., Cambridge Univ. Press, New York
Janev R., Langer W., Evans K., 1987, Elementary Processes in Hydrogen–Helium Plasmas – Cross Sections and Reaction Rate Coefficients. Springer, Berlin
Jeong K. S., Chang C., Sedlmayr E., Sülzle D., 2000, J. Phys. B: At. Mol. Opt. Phys., 33, 3417
Jeong K. S., Winters J. M., Le Bertre T., Sedlmayr E., 2003, A&A, 407, 191
Johnson R. D. I., 2018, NIST Computational Chemistry Comparison and Benchmark Database NIST Standard Reference Database Number 101, http://cccbdb.nist.gov/
Johns J. W. C., Priddle S. H., Ramsay D. A., 1963, Discuss. Faraday Soc., 35, 90
Johnston R. L., 2002, Atomic and Molecular Clusters, Master's Series in Physics and Astronomy, 1st edn., CRC Press, Florida (USA), https://www.taylorfrancis.com/books/9781420055771
Kamiński T. et al., 2016, A&A, 592, A42
Kamiński T. et al., 2017, A&A, 599, A59
Karakas A. I., 2010, MNRAS, 403, 1413
Karakas A., Lattanzio J. C., 2007, Publ. Astron. Soc. Aust., 24, 103
Khouri T. et al., 2016, A&A, 591, A70
Khouri T., Vlemmings W. H. T., Olofsson H., Ginski C., De Beck E., Maercker M., Ramstedt S., 2018, A&A, 620, 75
Köhler T. M., Gail H.-P., Sedlmayr E., 1997, A&A, 320, 553
Kramida A., Ralchenko Y., Reader J., NIST ASD Team, 2018, NIST Atomic Spectra Database (version 5.5.6). Natl. Inst. Stand. Technol.
Kurucz R., 1992, Rev. Mex. Astron. Astrofis., 23, 45
Lamiel-Garcia O., Cuko A., Calatayud M., Illas F., Bromley S. T., 2017, Nanoscale, 9, 1049
Langowski M. P. et al., 2015, Atmos. Chem. Phys, 15, 273
Lee G., Helling C., Giles H., Bromley S. T., 2015, A&A, 575, A11
Lee G. K. H., Blecic J., Helling C., 2018, A&A, 614, 126
Li R., Cheng L., 2012, Comput. Theor. Chem., 996, 125
Li G., Gordon I. E., Rothman L. S., Tan Y., Hu S.-M., Kassi S., Campargue A., Medvedev E. S., 2015, ApJS, 216, 15
Luo Y., 2007, Comprehensive Handbook of Chemical Bond Energies. CRC Press, Florida (USA), http://staff.ustc.edu.cn/ luo971/2010-91-CRC-BDEs-Tables.pdf
McElroy D., Walsh C., Markwick A. J., Cordiner M. A., Smith K., Millar T. J., 2013, A&A, 550, A36

McKinnon R., Vogelsberger M., Torrey P., Marinacci F., Kannan R., 2018, MNRAS, 478, 2851
McSween H. J., Huss G. R., 2010, Cosmochemistry. Cambridge Univ. Press, Cambridge
Martin W. C., Zalubas R., 1979, J. Phys. Chem. Ref. Data, 8, 817
Martin W. C., Zalubas R., 1983, J. Phys. Chem. Ref. Data, 12, 323
Martínez-Núñez E., Whalley C. L., Shalashilin D., Plane J. M. C., 2010, J. Phys. Chem. A, 114, 6472
Moore C. E., 1993, in Gallagher J. W., ed., CRC Ser. Eval. Data At. Phys. CRC Press, Boca Raton, FL
Nguyen A. N., Messenger S., 2009, Identification of an Extremely 18O-rich Presolar Silicate Grain in Acfer 094
Nittler L. R., Alexander C. M. O., Gao X., Walker R. M., Zinner E. K., 1994, Nature, 370, 443
Nittler L. R., Alexander C. M. O., Gao X., Walker R. M., Zinner E., 1997, ApJ, 483, 475
Nittler L. R., Alexander C. M. O., Gallino R., Hoppe P., Nguyen A. N., Stadermann F. J., Zinner E. K., 2008, ApJ, 682, 1450
Norris B. R. M. et al., 2012, Nature, 484, 220
Ohnaka K., Weigelt G., Hofmann K.-H., 2016, A&A, 589, A91
Oliphant T. E., 2006, A Guide to NumPy, Trelgol Publishing, p. 85
Patrascu A. T., Yurchenko S. N., Tennyson J., 2015, MNRAS, 449, 3613
Patzer A. B. C., Gauger A., Sedlmayr E., 1998, A&A, 337, 847
Patzer A. B., Chang C., Sedlmayr E., Sülzle D., 2005, Eur. Phys. J. D, 32, 329
Phillips J. G., 1971, ApJ, 169, 185
Plane J. M. C., 2013, Phil. Trans. R. Soc. A, 371, 20120335
Plane J. M. C., Helmer M., 1995, Faraday Discuss., 100, 411
Plane J. M. C., Whalley C. L., 2012, J. Phys. Chem. A, 116, 6240
Plane J. M. C., Feng W., Dawkins E. C. M., 2015, Chem. Rev., 115, 4497
Popovas A., Jørgensen U. G., 2016, A&A, 595, A130
Posch T., Kerschbaum F., Mutschke H., Fabian D., Dorschner J., Hron J., 1999, A&A, 352, 609
Poulaert G., Brouillard F., Claeys W., McGowan J. W., Wassenhove G. V., 1978, J. Phys. B: At. Mol. Phys., 11, L671
Ritter D., Weisshaar J. C., 1989, J. Phys. Chem., 93, 1576
Robitaille T. P. et al., 2013, A&A, 558, A33
Rollason R. J., Plane J. M. C., 2001, Phys. Chem. Chem. Phys., 3, 4733
Rothman L. et al., 2010, J. Q. Spectrosc. Radiat. Transfer, 111, 2139
Saloman E. B., 2012, J. Phys. Chem. Ref. Data, 41, 013101
Sarangi A., Cherchneff I., 2015, A&A, 575, A95
Savel'ev A. M., Starik A. M., 2018, Combust. Flame, 196, 223
Sharipov A. S., Loukhovitski B. I., 2018, Combust. Explos., 11
Sharipov A. S., Starik A. M., 2016, Chem. Phys., 465–466, 9
Sharipov A., Titova N., Starik A., 2011, J. Phys. Chem. A, 115, 4476
Sharipov A. S., Titova N. S., Starik A. M., 2012, Combust. Theory Model., 16, 842
Sierka M. et al., 2007, Angew. Chem. Int. Ed., 46, 3372
Sloan G. C., Levan P. D., Little-Marenin I. R., 1996, ApJ, 463, 310
Sloan G. C., Kraemer K. E., Goebel J. H., Price S. D., 2003, ApJ, 594, 483
Sluder A., Milosavljević M., Montgomery M. H., 2018, MNRAS, 480, 5580
Speck A. K., Barlow M. J., Sylvester R. J., Hofmeister A. M., 2000, A&AS, 146, 437
Starik A. M., Kuleshov P. S., Sharipov A. S., Titova N. S., Tsai C.-J., 2014, Combust. Flame, 161, 1659
Starik A. M., Savel'ev A. M., Titova N. S., 2015, Combust. Explos. Shock Waves, 51, 197
Stroud R. M., Nittler L. R., Alexander C. M. O., 2004, Science, 305, 1455
Stroud R. M., Nittler L. R., Alexander C. M. O., Zinner E., 2007, Lunar Planet. Sci. Conf., p. 2203
Suh S.-M., Zachariah M. R., Girshick S. L., 2001, J. Vac. Sci. Technol. A, 19, 940
Swihart M. T., Catoire L., Legrand B., Gökalp I., Paillard C., 2003, Combust. Flame, 132, 91
Takigawa A., Tachibana S., Nagahara H., Ozawa K., 2015, ApJS, 218, 2
Tanaka K. K., Tanaka H., Yamamoto T., Kawamura K., 2011, J. Chem. Phys., 134, 204313
Teyssandier F., Allendorf M. D., 1998, J. Electrochem. Soc., 145, 2167
The Astropy Collaboration, 2018, 156, 123
Toxvaerd S., 2015, J. Chem. Phys., 143, 154705
Tsai S.-M., Lyons J. R., Grosheintz L., Rimmer P. B., Kitzmann D., Heng K., 2017, ApJS, 228, 20
van Heijnsbergen D., Demyk K., Duncan M. A., Meijer G., von Helden G., 2003, Phys. Chem. Chem. Phys., 5, 2515
Verner D. A., Ferland G. J., 1996, ApJS, 103, 467
Vidler M., Tennyson J., 2000, J. Chem. Phys., 113, 9766
Wakelam V. et al., 2012, ApJS, 199, 21
Washburn E. B., Trivedi J. N., Catoire L., Beckstead M. W., 2008, Combust. Sci. Technol., 180, 1502
Whalley C. L., Plane J. M. C., 2010, Faraday Discuss., 147, 349
Whalley C. L., Martín J. C. G., Wright T. G., Plane J. M. C., 2011, Phys. Chem. Chem. Phys., 13, 6352
Woitke P., 2006a, A&A, 452, 537
Woitke P., 2006b, A&A, 460, 9
Wong A., Yurchenko S. N., Bernath P., Müller H. S. P., McConkey S., Tennyson J., 2017, MNRAS, 470, 882
Yurchenko S. N., Williams H., Leyland P. C., Lodi L., Tennyson J., 2018, MNRAS, 479, 1401
Zeidler S., Posch T., Mutschke H., 2013, A&A, 553, 81
Zhao-Geisler R., Köhler R., Kemper F., Kerschbaum F., Mayer A., Quirrenbach A., Lopez B., 2015, PASP, 127, 732

SUPPORTING INFORMATION

Supplementary data are available at *MNRAS* online.

online-material-accepted_version.pdf

Please note: Oxford University Press is not responsible for the content or functionality of any supporting materials supplied by the authors. Any queries (other than missing material) should be directed to the corresponding author for the article.

APPENDIX A: GIBBS FREE ENERGY

The GFE of a system is defined as

$$G = H - TS, \tag{A1}$$

where H is the enthalpy, S is the entropy, and T is the temperature of the system. The enthalpy is defined as

$$H = U + PV, \tag{A2}$$

where U is the internal energy of the system, P is the pressure of the system, and V is the volume of the system. Both entropy and internal energy depend on the configurational freedom of the particles in the system. This configurational freedom or statistical properties of a particle is described by its partition function. When dealing with a system of N non-interacting particles, the system's partition function is given by

$$Z_N = \frac{1}{N!} Z_1^N, \tag{A3}$$

where Z_1 is the partition function of a single particle.

The entropy for a system consisting of N particles is defined as

$$\begin{aligned} S_N &= \left. \frac{\partial kT \ln Z_N}{\partial T} \right|_{V,N} \\ &= k \ln Z_N + kT \left. \frac{\partial \ln Z_N}{\partial T} \right|_{V,N}. \end{aligned} \tag{A4}$$

Substituting Z_N using equation (A3) yields,

$$\begin{aligned} S_N &= Nk \ln Z_1 - k \ln(N!) + kT \left. \frac{\partial N \ln Z_1 - k \ln(N!)}{\partial T} \right|_{V,N} \\ &= Nk \ln Z_1 + NkT \left. \frac{\partial \ln Z_1}{\partial T} \right|_V - k \ln(N!) \\ &= N S_1 - k \ln(N!) \\ &\approx N S_1 - Nk \ln N + kN, \end{aligned} \tag{A5}$$

where the last transition uses Stirling's approximation that is valid for $N \gg 1$. As this quantity is often calculated for one mole ($6.022\,140\,758 \times 10^{23}$ particles), this is a valid approximation.

The internal energy of a system consisting of N particles is defined as

$$U_N = kT^2 \left. \frac{\partial \ln Z_N}{\partial T} \right|_{V,N}. \tag{A6}$$

Again, substituting Z_N with equation (A3), this reduces to

$$\begin{aligned} U_N &= NkT^2 \left. \frac{\partial \ln Z_1}{\partial T} \right|_V \\ &= N U_1. \end{aligned} \tag{A7}$$

Typically, the partition function is calculated with respect to the bottom of the particle's energy well (Section A1.4). Therefore, this energy value, U_0,[24] is separated from the partition function and equation (A7) becomes,

$$\begin{aligned} U_N &= NkT^2 \left. \frac{\partial \ln Z_1}{\partial T} \right|_V + N U_0 \\ &= N(U_1 + U_0). \end{aligned} \tag{A8}$$

Substituting equations (A2), (A5), and (A8) into (A1), combined with the ideal gas law, yields the GFE of a system of N particles,

$$G_N = N U_0 - NkT \ln Z_1 + NkT \ln N, \tag{A9}$$

which only depends on the total partition function of a single particle and U_0 of that particle.

A1 Partition functions of one particle

According to the Born–Oppenheimer approximation rotational, vibrational, and electronic energies are independent of each other, and the partition function of one particle can be written as the product of separate contributors namely translational, rotational, vibrational, and electronic degrees of freedom, $Z_1 = Z_{\rm tr} Z_{\rm rot} Z_{\rm vib} Z_{\rm el}$. This section contains a summary of all different partition function for the most general case of a non-linear poly atomic ideal gas, a linear poly atomic ideal gas, and a mono atomic ideal gas.

A1.1 Translation

The translational part is always given by

$$\begin{aligned} Z_{\rm tr} &= \left(\frac{2\pi mkT}{h^2} \right)^{3/2} V \\ &= \left(\frac{2\pi mkT}{h^2} \right)^{3/2} \frac{NkT}{P}, \end{aligned} \tag{A10}$$

where m is the mass of the particle and h is the Planck constant. Note that V is the volume of the embedding system meaning that N is the total number of particles of the system in which this one particle resides.

A1.2 Rotation

(I) Non-linear poly atomic

$$Z_{\rm rot} = \frac{1}{\sigma} \left(\frac{\pi T^3}{\Theta_x \Theta_y \Theta_z} \right)^{1/2}, \tag{A11}$$

where σ is the molecule's symmetry number,[25] and Θ_i the rotational temperature related to the moments of inertia, I_x, I_y, I_z, via

$$\Theta_i = \frac{\hbar^2}{2 I_i k} \qquad i \in \{x, y, z\}. \tag{A12}$$

(II) Linear poly atomic

$$Z_{\rm rot} = \frac{T \Theta_{\rm rot}}{\sigma}, \tag{A13}$$

where $\Theta_{\rm rot}$ is the rotational temperature related to the moment of inertia, I via

$$\Theta = \frac{\hbar^2}{2 I k}. \tag{A14}$$

(III) Mono atomic

$$Z_{\rm rot} = 0. \tag{A15}$$

Note that this is a high-temperature approximation that is valid when the temperature is much larger than rotational temperature, which is the case in all our simulations.

A1.3 Vibration

A molecules consisting of N atoms has $3N$ degrees of freedom, where the factor '3' corresponds to the possible movements of a particle in three-dimensional space. In the most general case, a molecule has $3N - 3 - 3 = 3N - 6$ vibrational degrees of freedom where the '-3' terms are the translational and rotational degrees of freedom of the molecule. We choose the zero-energy reference point as the bottom of the potential well and not the vibrational ground state.

(1) Non-linear poly atomic

$$Z_{\rm vib} = \prod_{\Theta_v \in \mathcal{T}_v} \frac{e^{-\Theta_v/2T}}{1 - e^{-\Theta_v/T}}, \tag{A16}$$

where Θ_v is the vibrational temperature related to a vibrational frequency ν of the molecule via

$$\Theta_v = \frac{h\nu}{k}, \tag{A17}$$

when assuming that the vibrational modes of the molecule behave like harmonic oscillators. $\mathcal{T}_v$ is the set of all $3N - 6$ vibrational modes of the molecule.

(2) Linear poly atomic

$$Z_{\rm vib} = \prod_{\Theta_v \in \mathcal{T}_v} \frac{e^{-\Theta_v/2T}}{1 - e^{-\Theta_v/T}}. \tag{A18}$$

[24] U_0 is the sum of the electronic ground state and nuclear–nuclear repulsion energies, isolated in vacuum, without vibration at 0 K.

[25] A molecule's symmetry number is the number of different but indistinguishable views of the molecule to correct for counting equivalent views.

Note that $\mathcal{T}_v$ only contains $3N - 5$ vibrational modes due to a rotational symmetry of the molecule.

(3) Mono atomic

$$Z_{\rm vib} = 0. \tag{A19}$$

A1.4 Electronic

The electronic part is always given by

$$Z_{\rm el} = \sum_{i=0}^{N_{\rm e}} g_i {\rm e}^{-\epsilon_i/kT}, \tag{A20}$$

with ϵ_i the ith electronic energy level w.r.t. the bottom of the electronic potential well, g_i the degeneracy of the ith level due to spin splitting, and $N_{\rm e}$ the number of energy levels. Each energy level can be scaled by choosing the bottom of the well to be 0,[26] giving $\varepsilon_i = \epsilon_i - \epsilon_0$. The number of levels can also be limited to the one where $\varepsilon_{N_{\rm lim}} \gg kT$.

$$Z_{\rm el} = g_0 + \sum_{i=1}^{N_{\rm lim}} g_i {\rm e}^{-\varepsilon_i/kT}. \tag{A21}$$

APPENDIX B: GIBBS FREE ENERGY OF FORMATION

Generally, the standard GFEoF, rather than the GFE, is used to determine reversed reaction rate coefficients under the assumption of detailed balance. Although both can be used, we opt for GFE for reason explained in the main text (Section 3.6.2) but explain GFEoF for completeness and comparison. The GFEoF of a compound is the change in GFE that occurs when one mole of the compound is formed from its component elements in their most thermodynamically stable states under standard conditions (pressure of 1 bar $= 1 \times 10^5$ Pa). Note that this state, depending on the components can be gaseous, solid, or liquid.

Consider a molecule m consisting of N unique atoms with each atom a occurring υ_a times in the molecule. Then, the set with unique atoms is defined as $\mathcal{A} = \{a_1, a_2, \ldots, a_N\}$. For an example molecule $m = {\rm H_2O}$, this gives $N = 2$, $\mathcal{A} = \{{\rm H}, {\rm O}\}$, $\upsilon_{\rm H} = 2$, and $\upsilon_{\rm O} = 1$. Following the documentation of GAUSSIAN09 (Frisch et al. 2013), the standard GFEoF of molecule m at a given temperature T, $\Delta_f G^\circ_{T,m}$, is described by

$$\Delta_f G^\circ_{T,m} = \Delta_f H^\circ_{T,m} - T\left(S^\circ_{T,m} - \sum_{a\in\mathcal{A}} \upsilon_a S^\circ_{T,a}\right), \tag{B1}$$

where $\Delta_f H^\circ_{T,m}$ is the standard enthalpy of formation[27] of molecule m at a given temperature, $S^\circ_{T,m}$ and $S^\circ_{T,a}$ are the entropy at a given temperature of molecule m and atom a, respectively. The $^\circ$ notation refers to the quantity at standard pressure of 1 bar ($= 1 \times 10^5$ Pa). The standard enthalpy of formation of molecule m at temperature T is described by

$$\Delta_f H^\circ_{T,m} = \Delta_f H^\circ_{0,m} + H^\circ_{T,m} - H^\circ_{0,m} - \sum_{a\in\mathcal{A}} \upsilon_a \left(H^\circ_{T,a} - H^\circ_{0,a}\right), \tag{B2}$$

where H°_T denotes the standard (thermal) enthalpy (equation A2) that excludes the electronic potential energy U_0[24] of the species. The standard enthalpy of formation of a molecule at absolute zero is given by

$$\Delta_f H^\circ_{0,m} = U_{0,m} + U_{{\rm zpve},m} - \sum_{a\in\mathcal{A}} \upsilon_a \left(U_{0,a} - \Delta_f H^\circ_{0,a}\right), \tag{B3}$$

where $U_{{\rm zpve},m}$ is the zero-point vibration energy of a molecule, which is the lowest vibrational energy (ground state) at 0 K. Note that this is not the bottom of the vibrational potential well (when representing this as harmonic oscillator potential). Combining equations B1, B2, and B3, and rearranging some terms, the standard GFEoF is given by

$$\Delta_f G^\circ_{T,m} = H^\circ_{T,m} - H^\circ_{0,m} + U_{0,m} + U_{{\rm zpve},m} - T S^\circ_{T,m} - \sum_{a\in\mathcal{A}} \upsilon_a \left(H^\circ_{T,a} - H^\circ_{0,a} + U_{0,a} - \Delta_f H^\circ_{0,a} - T S^\circ_{T,a}\right). \tag{B4}$$

When realizing that $H^\circ_{0,m} = U_{{\rm zpve},m}$ for a molecule and $H^\circ_{0,a} = 0$ for an atom, the standard GFEoF reduces to

$$\Delta_f G^\circ_{T,m} = H^\circ_{T,m} + U_{0,m} - T S^\circ_{T,m} - \sum_{a\in\mathcal{A}} \upsilon_a \left(H^\circ_{T,a} + U_{0,a} - \Delta_f H^\circ_{0,a} - T S^\circ_{T,a}\right). \tag{B5}$$

APPENDIX C: QUANTUM MECHANICAL DATA

This section contains an overview of all quantum mechanical data that was collected and calculated (Table C1 for the nucleation species and Table C2 for all other species). All gathered data has been homogenized and is available as a JSON file. A collection of

Table C1. Nucleation cluster specifications. All quantum mechanical properties of these clusters are calculated in this work (U_0, $Z_{\rm l}/Z_{\rm tr}$, $\Theta_{\rm rot}$, $\Theta_{\rm vib}$).

Cluster	Sizes	Global minimum	Monomer radius (nm)
TiO_2	1–10	Lamiel-Garcia et al. (2017)	0.162[a]
SiO	1–10	Bromley et al. (2016)	0.075765[b]
MgO	1–10	Chen, Felmy & Dixon (2014)	0.0865[c]
Al_2O_3	1–7	Li & Cheng (2012)	0.3304[d]
	8	Gobrecht et al. (2018)	

Note. All used monomer radii can be more accurate by accounting for the geometry of the non-linear molecules and using our re-evaluated structures (Section 6.1.1).

[a]Inter atomic Ti−O distance from Jeong et al. (2000).

[b]Half a Si−O bond length from Bromley et al. (2016).

[c]Half a Mg−O bond length from Farrow, Chow & Woodley (2014).

[d]Inter atomic distance O−Al−O (linear geometry) from Archibong & St-Amant (1999).

[26]This energy difference should be added again in the total internal energy of the molecule (equation A8).

[27]The standard enthalpy of formation of a compound is the change of enthalpy during the formation of one mole of that substance from its constituent elements, with all substances in their standard states. For an atom, this is the standard enthalpy of phase transition w.r.t. the phase in its standard state, i.e. the energy that must be supplied as heat at constant pressure per mole to convert from one phase to the other.

Table C2. Overview of the sources of all quantum mechanical data, either gathered or calculated, as defined in Appendix A.

Species	Global minimum	U_0	Z_1/Z_{tr}	Θ_{rot}, Θ_{vib}	ε_i
TiO	–	CCCBDB	Kurucz (1992)[a]	–	Phillips (1971)[c]
CO_2	–	CCCBDB	Rothman et al. (2010)[a]	–	Herzberg (1966)[e]
OH	–	CCCBDB	Rothman et al. (2010)[a]	–	Huber & Herzberg (1979)[e]
AlO	–	CCCBDB	Patrascu, Yurchenko & Tennyson (2015)[a]	–	–
AlH	–	CCCBDB	Yurchenko et al. (2018)[a]	–	–
NO	–	CCCBDB	Wong et al. (2017)[a]	–	Huber & Herzberg (1979)[e]
CO	–	CCCBDB	Li et al. (2015)[a]	–	–
SO	–	CCCBDB	Gamache et al. (2017)[b]	–	?[c]
SO_2	–	CCCBDB	Gamache et al. (2017)[b]	–	Herzberg (1966)[e]
HO_2	–	CCCBDB	Gamache et al. (2017)[b]	–	–
H_2O_2	–	CCCBDB	Gamache et al. (2017)[b]	–	–
O_2	–	CCCBDB	Gamache et al. (2017)[b]	–	Huber & Herzberg (1979)[e]
N_2	–	CCCBDB	Gamache et al. (2017)[b]	–	–
N_2O	–	CCCBDB	Gamache et al. (2017)[b]	–	Herzberg (1966)[e]
NO_2	–	CCCBDB	Gamache et al. (2017)[b]	–	?[e]
H_2O	–	CCCBDB	Furtenbacher et al. (2016)[f]	–	–
H_2	–	CCCBDB	Popovas & Jørgensen (2016)	–	Huber & Herzberg (1979)[e]
AlC	–	CCCBDB	✓	CCCBDB	–
AlH_2	–	CCCBDB	✓	CCCBDB	–
AlH_3	–	CCCBDB	✓	CCCBDB	–
HCO	–	CCCBDB	✓	CCCBDB	Johns, Priddle & Ramsay (1963)[e, g]
HO_2	–	CCCBDB	✓	CCCBDB	Becker et al. (1978)[e, h]
MgO	–	CCCBDB	✓	CCCBDB	Bauschlicher & Schwenke (2017)[i], Huber & Herzberg (1979)[e]
MgOH	–	CCCBDB	✓	CCCBDB	–
$Mg(OH)_2$	–	CCCBDB	✓	CCCBDB	–
$MgCO_3$	–	CCCBDB	✓	CCCBDB	–
O_3	–	CCCBDB	✓	CCCBDB	–
SiO_2	–	CCCBDB	✓	CCCBDB	–
AlO_2	Patzer et al. (2005)	✓	✓	✓	–
Al_2O	Patzer et al. (2005)	✓	✓	✓	–
Al_2O_2	Patzer et al. (2005)	✓	✓	✓	–
AlOH	✓	✓	✓	✓	–
AlO_2H	✓	✓	✓	✓	–
$Al(OH)_2$	✓	✓	✓	✓	–
$Al(OH)_3$	✓	✓	✓	✓	–
H	✗	CCCBDB	✗	✗	-
C	✗	CCCBDB	✗	✗	Haris & Kramida (2017); Beckmann et al. (1975)[d]
Mg	✗	✓	✗	✗	-
N	✗	✓	✗	✗	-
O	✗	✓	✗	✗	Moore (1993)[d]
Si	✗	✓	✗	✗	Martin & Zalubas (1983)[d]
Al	✗	✓	✗	✗	Martin & Zalubas (1979)[d]
Ti	✗	✓	✗	✗	Saloman (2012)[d]

Note. ✓: This work, ✗: not applicable, -: unnecessary, ?: no references provided, CCCBDB: NIST Computational Chemistry Comparison and Benchmark Database (Johnson 2018).
[a]Via ExoMol (http://exomol.com/).
[b]Via HITRAN (Gordon et al. 2017).
[c]Via NIST chemistry WebBook (https://doi.org/10.18434/T4D303).
[d]Via NIST Atomic Spectra Database (Kramida et al. 2018).
[e]Via CCCBDB (Johnson 2018).
[f]Uses $g = 1$ and $g = 3$ as para–ortho degeneracy that is preferred over using $g = 1/4$ and $g = 3/4$ like Vidler & Tennyson (2000).
[g]The most likely reference of list of the references provided by NIST chemistry WebBook (https://doi.org/10.18434/T4D303).
[h]Unclear reference for the second energy level.
[i]First level: improved theoretical value over the theoretical one of Huber & Herzberg (1979).

used literature input files (raw and cleaned versions), reference files, and info files is also available online.[28] All this data was used to calculate GFEs, which are also available online for the temperature range on our interest 500–3000 K at standard pressure of 1 bar, which also have been included in KROME. Adaptations of these tables can easily be produced with our open-source repository[29] and the provided data.

[28]Zenodo: doi.org/10.5281/zenodo.3356710

[29]https://bitbucket.org/JelsB/thermochemistry

APPENDIX D: RESULTS

This appendix encompasses additional figures of the nucleation models (Supplementary online material). Figures that are not shown in this appendix are either already present in the main body or provide no added value.

D1 Closed nucleation networks

This section contains a more thorough overview of all closed nucleation models of all nucleation clusters results.

D1.1 Monomer nucleation

This section contains a more complete overview of the closed nucleation models using the MN description of all nucleation clusters results.

TiO_2-clusters: Figs D1 to D2
MgO-clusters: Figs D3 to D5
SiO-clusters: Fig. D6
Al_2O_3-clusters: Figs D7 to D9

D1.2 Polymer nucleation

This section contains a more complete overview of the closed nucleation models using the PN description of all nucleation clusters results.

TiO_2-clusters: Figs D10 to D11
MgO-clusters: Figs D12 to D14
SiO-clusters: Fig. D15
Al_2O_3-clusters: Figs D16 to D18

D1.3 Polymer nucleation compared with equilibrium

This section contains figures that compare the relative ratios of nucleation clusters of the closed nucleation models w.r.t. the equilibrium ratios (Figs D19 to D21).

D2 Comprehensive chemical nucleation networks

This section contains a more complete overview of all nucleation clusters results in the comprehensive chemical nucleation model using the PN description. No Mg-related figures are shown as it remains completely atomic.

D2.1 Ti-bearing species

This section contains a more complete overview of all Ti-bearing species results in the comprehensive chemical nucleation model using the PN description (Figs D22 and D23).

D2.2 Si-bearing species

This section contains a more complete overview of all Si-bearing species results in the comprehensive chemical nucleation model using the PN description (Fig. D24).

D2.3 Al-bearing species

This section contains a more complete overview of all Al-bearing species results in the comprehensive chemical nucleation model using the PN description (Figs D25 and D26).

APPENDIX E: CHEMICAL NETWORK

This appendix lists all the used reactions with their reaction rate coefficient and the source of this data (Supplementary online material). This is the comprehensive chemical network used in this paper. Subsets of this network are not explicitly listed, i.e. the closed nucleation networks.

References: (1) Washburn et al. (2008), (2) Sharipov et al. (2012), (3) Starik et al. (2014), (4) Sharipov et al. (2011), (5) Sharipov & Starik (2016), (6) This work, (7) Swihart et al. (2003), (8) UMIST data base McElroy et al. (2013) , (9) KIDA data base Wakelam et al. (2012), (10) Verner & Ferland (1996), (11) Janev et al. (1987), (12) Forrey (2013), (13) Glover & Abel (2008), (14) DeMore et al. (1997), (15) Abel et al. (1997), (16) Poulaert et al. (1978), (17) Capitelli et al. (2007), (18) Glover et al. (2010), (19) Verner & Ferland (1996), (20) Plane et al. (2015), (21) Whalley et al. (2011), (22) Plane & Whalley (2012), (23) Plane & Helmer (1995), (24) Rollason & Plane (2001), (25) Langowski et al. (2015), (26) Atkinson et al. (2004), (27) Campbell & McClean (1993), (28) Ritter & Weisshaar (1989), (29) Higuchi et al. (2008), and (30) Plane (2013).

This paper has been typeset from a TEX/LATEX file prepared by the author.